

1
2
3 **A model-based diagnostic technique to enhance faults isolability in**
4
5
6 **Solid Oxide Fuel Cell systems¹**
7

8
9 Pierpaolo Polverino^{*,a}, Marco Sorrentino^a, Cesare Pianese^a

10
11 ^a*Università degli Studi di Salerno, via Giovanni Paolo II 132, 84084, Fisciano (SA), ITALY*

12
13 *Corresponding author: e-mail ppolverino@unisa.it, Tel. +39 089 96 4178, Fax. +39 089 96 4037.
14
15

16 **Abstract**
17

18 This work illustrates an innovative diagnostic technique able to improve fault isolability in Solid Oxide
19 Fuel Cell (SOFC) energy conversion systems. On-board sensor reduction may induce fault clustering and,
20 thus, hinder univocal fault isolation. According to the proposed technique, isolated system component sub-
21 models, fed with faulty inputs, can be used to solve this issue. These models provide a set of redundant
22 residuals, which react only if the related component is under faulty state. The technique is characterized and
23 tested in simulated environment on an SOFC Anode Off-Gas Recycling (AOGR) system. Hydrogen external
24 leakage, fuel and air heat exchangers efficiency reduction and recirculation unit malfunction are addressed
25 and implemented in the complete system model. This latter is used to simulate system variables in both
26 nominal and faulty conditions and compute residuals for fault detection and isolation. The sub-models are
27 then used to introduce further residuals, and their behaviour is investigated at different fault magnitudes. The
28 analysis is firstly performed in an ideal case scenario, considering the fault isolability that can be
29 theoretically achieved. Then, practical application of the diagnostic algorithm is discussed, considering
30 quantitative residuals deviation and properly analysing the effects of feeding the sub-models with inputs
31 provided by both faulty and nominal models. The achieved results confirm the capability of the proposed
32 approach to univocally isolate the considered faults in all the investigated conditions. Moreover, the analysis
33 of the real case scenario proved the proposed algorithm suitable also for real applications.
34
35
36
37
38
39
40
41
42
43
44
45
46
47
48
49
50
51
52
53

54 *Keywords: Solid Oxide Fuel Cell; Fault Detection; Fault Isolation; Model-based Diagnosis; Fault*
55 *Simulation; Diagnostic technique.*
56
57
58

59
60 ¹ The short version of the paper was presented at ICAE2016 on Oct 8-11, Beijing, China. This paper is a substantial
61 extension of the short version of the conference paper.
62

1. Introduction

Nowadays, Solid Oxide Fuel Cells (SOFCs) represent one of the most suitable alternatives to conventional energy production systems (e.g. internal combustion engines based on fossil fuels) for cogeneration and Auxiliary Power Unit (APU) uses [1]. However, SOFC mass-market deployment is mainly hindered by their high production costs and limited durability [2]. To overcome these issues, advanced control and diagnostic algorithms can be applied, since the use of proper diagnostic strategies can efficiently detect and isolate malfunctions at both stack and system levels [3]. Combining the diagnostic inference with suitable control strategies, appropriate counteractions can be implemented to prevent performance losses and abrupt system failure [4], thus reducing maintenance costs and improving system lifetime. This latter can also be increased using prognostic algorithms, able to perform online Remaining Useful Life (RUL) forecast by means of degradation mechanisms modelling [5] and proper use of control rules and diagnosis results [6].

Fuel cell manufacturing companies are mainly focusing on the improvement of overall system efficiency through advanced system configurations. Among those investigated, Anode Off-Gas Recycling (AOGR) has been singled-out as one of the most promising configurations, which is able to improve efficiency by increasing fuel utilization [7]. Nevertheless, such configuration implies the introduction of a recirculation unit and related balance of plant, with a consequent increase in system complexity and cost. In order to reduce this latter, manufacturers are also trying to decrease the number of sensors the system is equipped with. However, the reduction in available sensors may hinder the effectiveness of on-board diagnosis, since the source of key information is diminished [8]. For this reasons, it is clear the need for advanced diagnostic algorithms, able to use in a more efficient way the available measurements and boost information extraction with limited available equipment.

The present paper illustrates an innovative solution to the sensors reduction issue, by means of isolated sub-model analysis. The proposed technique allows achieving optimal fault detection and isolation at system component level, even though a reduced number of sensors is used. The main contribution given by the present paper to the available literature consists in the proposed diagnostic methodology, which uses in a more suitable way sensors measurements and system components models to amplify the available information and thus increase diagnostic redundancy.

1
2 In the following sections, an overview of the current State-of-the-Art concerning SOFC system
3 applications and diagnosis is presented, to highlight the originality and innovations of the present
4 manuscript. Then, a brief introduction to model-based diagnosis is given, followed by the description of the
5 proposed technique by means of a theoretical example. Afterwards, the technique is firstly applied to an
6 SOFC AOG system, then its efficacy is verified through simulation tests. As first step, the approach is
7 qualitatively investigated in an ideal case, and then its performance are examined in a realistic scenario,
8 introducing practical application limitations. In this latter case, quantitative analysis of the diagnostic results
9 is performed, highlighting the changes with respect to the ideal case.

10 11 12 13 14 15 16 17 **2. State-of-the-Art analysis on SOFCs applications and diagnosis**

18 19 20 2.1 Solid Oxide Fuel Cells applications overview

21
22 Several studies available in the literature investigate the use of SOFCs for Combined Heat and Power
23 (CHP) production [9][13], as APUs for ships [14][15] and trucks [16]-[18], combined with Gas Turbines
24 (GT) [19][24] as well as for fuel production (e.g. as electrolyzers) [25][27].

25
26
27
28
29 Concerning CHP systems, Ellamla et al. [9] detailed in their review on worldwide systems deployment
30 that, at the end of 2014, almost 100,000 units have been installed in Japan and around 1,000 units in South
31 Korea and Europe, respectively, with SOFCs covering about 10% of the total amount. Their robustness with
32 respect to load dynamics was proved by Hanke et al. [10], who tested SOFC stacks under power cycling
33 operation and observed no acceleration in the degradation rate compared to constant operation. This
34 advantage, associated to high energy conversion efficiency (and thus low fuel consumption with respect to
35 other fuel cell technologies), make SOFC systems appealing from both a technical and economic point of
36 view. Indeed, Napoli et al. [11] and Pellegrino et al. [12] observed that, although SOFCs shows high
37 investment costs, they ensure high yearly savings, at different configurations and load scenarios. On the
38 same line, Facci et al. [13] performed a techno-economic analysis of an SOFC-based power plant for the
39 combined generation of cooling, heat and electric power. Different configurations have been considered,
40 each one with a specific control strategy and optimal design, confirming in all cases a cost reduction with
41 respect to separate energy production systems.

42
43
44
45
46
47
48
49
50
51
52
53
54
55
56
57
58 In the work of Strezza et al. [14], a Life Cycle Assessment (LCA) method has been applied to a 20 kW
59 electric SOFC system operating as an APU, proving better environmental performances with respect to
60

1 conventional power systems (i.e. engines). Also Diaz-de Baldasano et al. [15] demonstrated the reduction in
2 pollutant emissions, combining a new designed SOFC system with diesel generators for ship uses.
3 Venkataraman et al. [16] developed a model of an SOFC APU coupled with a Vapour Absorption
4 Refrigerator System (VARS) for truck refrigeration, showing the feasibility of such an application for small
5 trucks, with a theoretical increase in the SOFC system efficiency up to 80% and a significant reduction in the
6 main engine load. In addition, the works of Kendall et al. [17] and Recheberg et al. [18] remarked the
7 advantage of using SOFCs for truck applications. The former focuses on the use of downsized microtubular
8 SOFC stacks running on Liquid Natural Gas (LNG), to improve system robustness and achieve faster
9 dynamic response, whereas the latter investigates heavy duty truck idling reduction by means of SOFCs as
10 APUs running on diesel fuel.

11 The coupling of SOFCs with GTs has also proved being effective. He et al. [19] illustrated that, through
12 the development of a suitable control strategy, substantial increase in system efficiency and power
13 management can be achieved. The work of Larosa et al. [20] details, through a simulation study, the
14 feasibility of developing a hybrid system made of an SOFC and a micro GT, whereas Santin et al. [21]
15 performed a thermo-economic analysis to investigate the main advantages related to an SOFC-GT hybrid
16 system with different fuels and plant configurations. Obara [22] accomplished a numerical investigation on
17 the electric stabilization of a 1.4 MW SOFC-based power plant (made of an SOFC, a GT and a steam
18 turbine) combined with a large scale photovoltaic plant. In the work of Zaccaria et al. [23], a 1-D real time
19 model of an SOFC has been coupled with GT equipment to assess the impact of cold air bypass on system
20 performance, aiming at safety operation and efficiency optimization. In addition, the analysis performed by
21 Sharifzadeh et al. [24] aimed at defining optimal trade-off among safety, flexibility and economy of a Triple
22 Combined-cycle Power Generation (TCPG) plant made of an SOFC stack (to produce steam and electricity
23 from syngas) and a combined cycle GT (to convert the thermal energy of the SOFC outlet gases into
24 electricity).

25 Solid oxide technology applied to fuel production processes is also widely investigated in the literature.
26 An example is given by the work of Cinti et al. [25], who investigated the integration of a Fischer-Tropsch
27 process with a Solid Oxide Electrolyser Cell (SOEC) stack for the production of liquid fuel with different
28 layouts. Moreover, new materials for SOFCs and SOECs have been analysed by Bi et al. [26] and Jung et al.

1 [27]: the former studied the introduction of proton-conducting oxides as electrolytes, whereas the latter the
2 implementation of new oxygen electrode materials, both remarking the main properties and used materials
3 (being key factors for economic feasibility of the technologies).
4
5

6 As already asserted in Section 1, SOFC AOGR systems are considered quite effective in improving fuel
7 cell efficiency and overall system performance, remarking the high interest shown by both research and
8 industrial community for such systems. However, the works available in the literature mainly entail system
9 design [7][28][31] and optimization [32][33], rather than control and diagnosis. In their studies, Terayama et
10 al. performed an assessment on the performance improvement of a disc-type SOFC associated to an AOGR
11 configuration, first experimentally [7] and then combining experiments and simulation analysis [28]. They
12 observed that the cell efficiency can increase between 2.5 and 3.3 times more than the case without AOGR,
13 acting on recycle rate, fuel utilization and cell temperature. A further benefit on cell resistance was also
14 observed through impedance measurements. In addition, Peters et al. [29] investigated the improvement
15 achieved by combining AOGR with dead-end loop configuration, achieving an efficiency of 61% with a fuel
16 utilization of 60%. Henke et al. [30] proposed a numerical analysis of the interaction between recirculation
17 rate and fuel utilization at stack and system level of both SOFC and SOEC systems, with particular attention
18 to carbon deposition rate change. They observed that high recirculation rates, combined with high fuel
19 utilization, reduces carbon formation in SOFCs, whereas low recirculation rates are better for SOECs, since
20 they prevent nickel oxidation. In the work of Tallgren et al. [31], a fuel feeder is developed to reproduce the
21 effect of AOGR configuration on a laboratory single-cell test station. The papers of Curletti et al. [32] and
22 Khani et al. [33] present a techno-economic analysis on a biogas fed SOFC power plant, the former, and on
23 an SOFC-GT cogeneration system, the latter, both showing AOGR configurations.
24
25

26 2.2 Overview on SOFC diagnosis

27 In the current literature, several papers apply diagnostic techniques to SOFC systems. For instance, Sorce
28 et al. [34] developed a model-based diagnostic algorithm to detect and isolate several faults at system level,
29 that are air leakage, fuel leakage, stack degradation and reformer degradation. They assessed algorithm
30 performance through simulation analysis and, afterwards, developed mathematical maps to represent system
31 behaviour in the investigated conditions for quick fault detection and isolation uses. Following a similar
32 approach, Greco et al. [35] combined model simulation and experimental results to characterize SOFC
33
34
35
36
37
38
39
40
41
42
43
44
45
46
47
48
49
50
51
52
53
54
55
56
57
58
59
60
61
62
63
64
65

1 system performance under reformer fault. The achieved results allowed the development of fault maps to be
2 used for diagnostic purposes. The faults accounted in [34] have been also considered in the works of
3
4 Costamagna et al. where model-based diagnostic algorithms, based on Support Vector Machine (SVM) [4]
5
6 and Random Forest (RF) [36] classification approach were proposed and analysed in simulated environment.
7

8
9 Pahon et al. [37] developed a signal-based diagnostic algorithm by means of wavelet transform applied to
10 SOFC stack voltage to detect abnormal operating conditions and assess, in each case, the stack state of
11 health. In the work of Sorrentino et al. [38], a Recurrent Neural Network (RNN) and a stepwise multiple
12 regression analysis have been used to develop a fault classifier able to distinguish between high temperature
13 gradients and anode re-oxidation. Also Pohjoranta et al. [39] used an RNN to design an algorithm, validated
14 in a simulated environment, for detecting voltage deviation of an SOFC multi-stack power plant. On the
15 other hand, Wu and Liu [40] used a supervised Self-Organization Map (SOM) model to develop two-
16 dimensional maps, with faults lying in specific space regions, to perform single and multiple fault detection
17 and isolation. A diagnostic algorithm based on least-square SVM was instead used in the work of Wu and Ye
18 [6], in combination with hidden semi-Markov models to perform SOFC RUL estimation under anode
19 poisoning and cathode humidification fault. Marra et al. [41] developed a lumped dynamic model of a 10 kW
20 SOFC stack installed into an AOGR system, detecting stack leakage by comparing simulated and measured
21 anode outlet gas concentrations. A leakage occurring at stack level was also studied by Halinen et al. [42],
22 who proposed an experimental method for leakage identification, aiming at manufacturing quality
23 assessment and fault diagnosis.
24
25
26
27
28
29
30
31
32
33
34
35
36
37
38
39
40
41

42 In the work of Polverino et al. [3], the authors proposed a model-based diagnostic algorithm relying on a
43 Fault Signature Matrix (FSM), developed combining Fault Tree Analysis (FTA) and fault simulation study.
44 The accounted faults occurring at SOFC system level relate to air blower fault, air leakage, temperature
45 controller failure, pre-reformer malfunction and stack fault. The proposed algorithm was firstly assessed in a
46 simulated environment and then applied to a real commercial micro-CHP system, as described in [8]. In this
47 latter work, the authors demonstrated the unfeasibility of performing univocal fault isolation under sensor
48 reduction problem, and, with the present paper, a suitable solution to such an issue is provided, bridging the
49 gap of such analysis in the available literature.
50
51
52
53
54
55
56
57
58
59
60
61
62
63
64
65

1 The present work focuses on the design of a model-based diagnostic technique oriented towards SOFC
2 AOGF systems, based on isolated sub-model analysis. Nevertheless, the proposed approach is quite general
3 and can be applied in a straightforward way to any kind of complex system, if proper component models are
4 available. Indeed, as thoroughly shown in Section 2.1, the use of SOFCs is addressed to many applications,
5 and the proposed technique would be of advantage for system performance improvement and overall cost
6 reduction in any investigated configuration.
7
8
9
10
11

12 **3. Proposed diagnostic technique**

13 3.1 Model-based diagnosis overview

14
15
16
17
18 System fault diagnosis aims at detecting and isolating abnormal component behaviours, which affect
19 system performance and may lead to gradual or abrupt system failure. Many approaches can be used for fault
20 diagnosis, and they are usually gathered under model- and signal-based methods [43]. The former uses
21 mathematical models, representing the process under analysis, to simulate system variables and compute
22 residuals, whereas the latter extracts significant performance indicators through a suitable post-processing of
23 system measurements [44]. It is worth observing that signal-based techniques may require a limited
24 knowledge about the analysed system/process but need large amount of experimental data to characterize the
25 diagnostic algorithm, with several issues concerning faulty data availability (i.e. lack of data, unfeasibility of
26 tests in specific faulty conditions, high cost and complexity of the experiments, etc.) [45]. Therefore,
27 although requiring a deeper awareness of the modelled phenomena, model-based techniques can be applied
28 to several systems and applications with slight modifications and limited amount of experimental data, since
29 their design is mostly based on physical principles and system identification techniques [46].
30
31
32
33
34
35
36
37
38
39
40
41
42
43
44

45 According to model-based approaches, residuals are usually related to specific system variables and
46 computed as the difference between their available measurements and simulated quantities. They are used to
47 detect any possible deviation of these monitored variables from defined reference (i.e. nominal) operations.
48 To achieve undesired (i.e. faulty) states detection, the residuals are compared to specific threshold ranges: if
49 a residual falls within the defined range, the related variable is considered behaving normally, otherwise an
50 anomalous event may be taking place [3]. To identify the location of the fault in the system, each residual
51 can be associated to an analytical symptom: this parameter is 0 when the residual shows a normal behaviour
52 (e.g. lays within the defined threshold range) and 1 otherwise (e.g. during faulty events). The link among the
53
54
55
56
57
58
59
60
61
62
63
64
65

1 symptoms and a set of possible occurring faults can be defined following an FTA approach, whose outcome
2 consists in an FSM [47]. Usually, an FSM shows on the rows the list of the considered faults, whereas on the
3 columns all the symptoms related to the monitored variables (i.e. residuals). If a i -th fault affects a j -th
4 symptom, the corresponding (i,j) -th matrix cell presents a 1, otherwise a 0. By comparing the symptoms
5 collected from system monitoring process with those listed in FSM rows, the correct isolation of the fault is
6 fulfilled if a perfect match is obtained.
7
8
9
10
11

12
13 Clearly, a reduction in the monitored variables, due to, e.g., less installed sensors, could prevent univocal
14 fault isolation: indeed, the reduction in available symptoms may lead two or more faults to show the same
15 pattern and collapse into fault clusters. As illustrated in Section 2.2, a proof of this observation was already
16 given by the authors, who verified in [8] that the use of a conventional diagnostic algorithm, designed in [3]
17 over a larger number of measurements, was not effective with few system measurements, since the univocal
18 isolation of faults was hindered by fault clustering.
19
20
21
22
23
24
25

26 In the following section, an innovative model-based diagnostic approach, which can improve fault
27 isolability under limited sensors number, is illustrated. Differently from other algorithms available in the
28 literature, isolated system components modelling is here proposed, so as to increase the number of computed
29 residuals and, thus, enhance information redundancy (i.e., more symptoms are generated). In this way, the
30 proposed approach can improve fault diagnosis with given number of installed sensors, or as well maintain
31 highly diagnostic efficiency also under sensors reduction issue.
32
33
34
35
36
37
38
39

40 3.2 Isolated sub-model analysis

41
42 The proposed approach is illustrated with respect to the generic system scheme shown in Fig. 1-a. The
43 considered system is characterized by two main components, namely P_1 and P_2 . The component P_1 presents
44 two measured input variables, u and z , and two measured output variables, x and y . The component P_2 shows
45 one measured input x and one measured output z . It is worth observing that the proposed scheme shows a
46 mutual interaction between the considered components, since the P_2 output z is a P_1 input, introducing a
47 complexity typical of an AOGR system (see Fig. 4 afterwards). It is here assumed that both components can
48 be affected by one fault each, generically referred as f_1 for the component P_1 and f_2 for P_2 . The system
49 components P_1 and P_2 are represented in normal (i.e. unfaulty) behaviour by the constitutive relations listed
50 in Table 1: component P_1 is characterized by the transfer functions g_{11} and g_{12} , whereas component P_2 by g_2 .
51
52
53
54
55
56
57
58
59
60
61
62
63
64
65

It is worth noting that these functions summarize the real physical relations among inputs and outputs and define the system components features as they should be in unfaulty conditions.

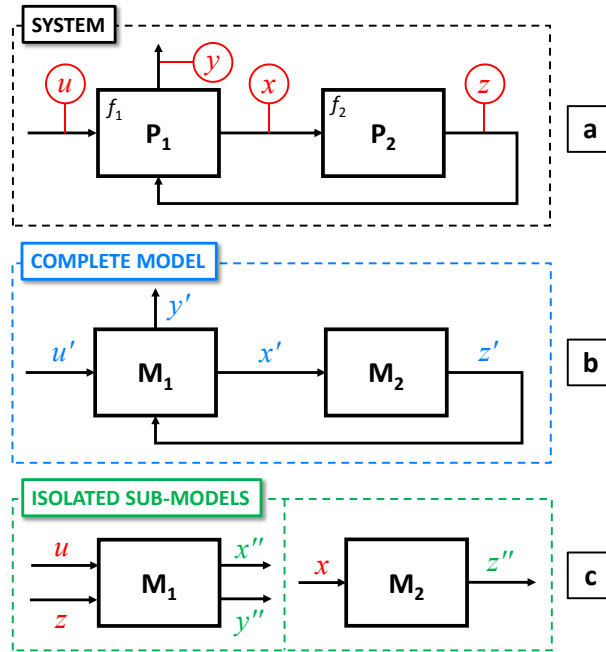


Fig. 1: System scheme (a) with two components, P_1 and P_2 , each one affected by a distinct fault; complete model simulation scheme (b), with model blocks M_1 and M_2 representing the corresponding system components; isolated sub-models simulation scheme (c).

As illustrated in Section 3.1, model-based diagnosis requires a suitable mathematical model to compute residuals. Therefore, a complete system model is here conceived, whose scheme is presented in Fig. 1-b. The model is composed by two sub-models, M_1 and M_2 , representative of the two system components P_1 and P_2 , respectively. Sub-model M_1 is defined through the transfer functions h_{11} and h_{12} and shows two inputs (u' and z') and two outputs (x' and y'), whereas sub-model M_2 is represented by the transfer function h_2 and has one input x' and one output z' . The constitutive relations among the simulated variables of the complete system model are listed as well in Table 1.

Table 1: Constitutive relations of the proposed system and model components.

Event	System	Complete Model	Isolated Sub-models
Unfaulty	$P_1 : \begin{cases} x = g_{11}(u, y, z) \\ y = g_{12}(u, x, z) \end{cases}$ $P_2 : \{ z = g_2(x) \}$	$M_1 : \begin{cases} x' = h_{11}(u', y', z') \\ y' = h_{12}(u', x', z') \end{cases}$ $M_2 : \{ z' = h_2(x') \}$	$M_1 : \begin{cases} x'' = h_{11}(u, y, z) \\ y'' = h_{12}(u, x, z) \end{cases}$ $M_2 : \{ z'' = h_2(x) \}$
Fault f_1	$P_1 : \begin{cases} x = g_{11}^f(u, y, z) \\ y = g_{12}^f(u, x, z) \end{cases}$ $P_2 : \{ z = g_2(x) \}$	Same as unfaulty	Same as unfaulty
Fault f_2	$P_1 : \begin{cases} x = g_{11}(u, y, z) \\ y = g_{12}(u, x, z) \end{cases}$ $P_2 : \{ z = g_2^f(x) \}$	Same as unfaulty	Same as unfaulty

3.2.1 Residuals generation through complete model

Assuming that the model input u' is a known and controlled input (i.e. $u' = u$) and neglecting measurement noise effects, a set of residuals, required for fault detection, is generated from the available measurements and modelled variables as follows:

$$\begin{aligned}
 r_1 &= x - x' = g_{11}(u, y, z) - h_{11}(u, y', z') \\
 r_2 &= y - y' = g_{12}(u, x, z) - h_{12}(u, x', z') \\
 r_3 &= z - z' = g_2(x) - h_2(x')
 \end{aligned} \tag{1}$$

From a general point of view, the model transfer functions are a mathematical approximation of the real system behaviour: they are usually affected by errors and model uncertainties and they can therefore differ from real system behaviour. However, in the presented example, these aspects are neglected and the models transfer functions are assumed being equal to the corresponding system ones during unfaulty conditions: this means that any change between model and system transfer functions is only due to faulty events occurring in the system. According to the previous assumption, the unfaulty condition can be represented through the logic sequence shown in Fig. 2-i, which induces the residuals depicted in equation (1) to be all 0.

During faulty operation, the transfer functions of the system component affected by the fault can change.

On the one hand, in case fault f_1 affecting component P_1 occurs, it is here assumed that both transfer functions g_{11} and g_{12} become $g_{11}^f \neq g_{11}$ and $g_{12}^f \neq g_{12}$, respectively, and that of the component P_2 remains unchanged. On the other hand, if fault f_2 occurs, the transfer function g_2 of the component P_2 becomes $g_2^f \neq g_2$, whereas those of P_1 do not vary. It is worth remarking that this study is performed assuming only one fault occurring at a time. The transfer function variations associated to the two faults are clearly illustrated in Table 1 and the related logic sequences are shown in Fig. 2-ii and Fig. 2-iii, respectively. The logical relations highlighted with dotted edges represent the unchanged conditions with respect to unfaulty state. According to these sequences, it is straightforward to assert that, in any faulty event, all the residuals evaluated in equation (1) diverge from their unfaulty behaviour (i.e. from 0).

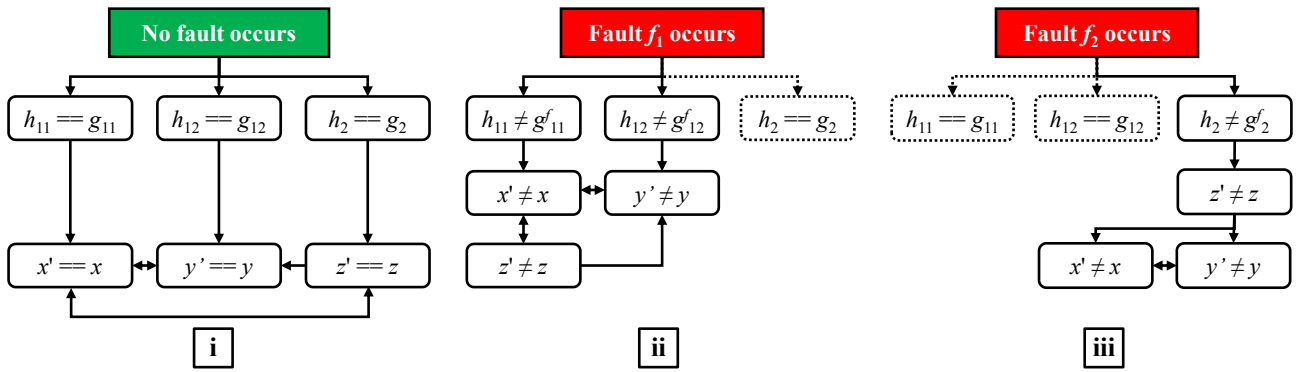


Fig. 2: Logic sequence for unfaulty conditions (i), fault f_1 occurrence (ii) and fault f_2 occurrence (iii) with respect to system and complete model; in faulty logic sequences, logical relations with dotted edges represent unchanged conditions with respect to unfaulty state.

This conclusion leads to the FSM illustrated in Table 2, where the two rows refer to fault f_1 and fault f_2 , respectively. Each symptom is related to the corresponding residual (i.e. symptom s_1 is linked to residual r_1 , and so on). It is evident that both fault signatures show the same symptoms pattern, proving that a limited number of symptoms may not be sufficient to fulfil univocal fault isolation.

Table 2: Fault Signature Matrix based on the residuals computed in equation (1) and the logic sequences illustrated in Fig. 2.

Event	Symptom s_1	Symptom s_2	Symptom s_3
Fault f_1	1	1	1
Fault f_2	1	1	1

3.2.2 Residual generation adding isolated sub-models

To solve this issue, sub-models M_1 and M_2 can be decoupled and analysed independently. The aim of this approach is to increase the number of residuals and symptoms, so as to achieve correct fault isolation. The sub-models are still represented through the transfer functions defined for the complete model, but each sub-model is fed with measured inputs (provided by the real system) instead of simulated ones (as done in the complete model). Indeed, according to the scheme shown in Fig. 1-c, the sub-model M_1 shows two measured inputs, u and z , and two simulated outputs, x'' and y'' , whereas the sub-model M_2 has one measured input x and one simulated output z'' .

As for the other cases, the constitutive relations for the sub-models are illustrated in Table 1, and through them the following residuals can be defined:

$$\begin{aligned}
 r_4 &= x - x'' = g_{11}(u, y, z) - h_{11}(u, y, z) \\
 r_5 &= y - y'' = g_{12}(u, x, z) - h_{12}(u, x, z) \\
 r_6 &= z - z'' = g_2(x) - h_2(x)
 \end{aligned} \tag{2}$$

Recalling that model errors and uncertainties are neglected, the unfaulty condition represented through the logic sequence in Fig. 2-i can be updated with respect to the new variables simulated through the isolated sub-models, as shown in Fig. 3-i. In this figure, three additional logic connections (sketched with light colour edges) are introduced. From the defined sequence, it is straightforward to assess that also the residuals defined in equation (2) are all 0 during unfaulty conditions.

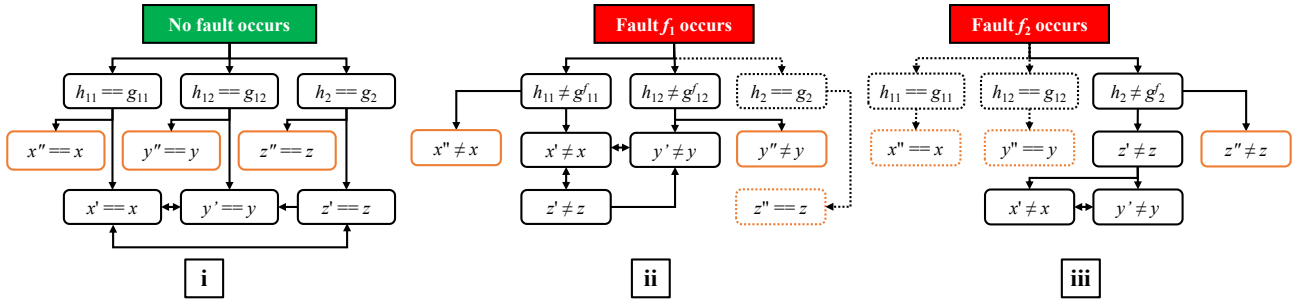


Fig. 3: Logic sequence for unfaulty conditions (i), fault f_1 occurrence (ii) and fault f_2 occurrence (iii) with respect to system, complete model and isolated sub-models; in faulty logic sequences, logical relations with dotted edges represent unchanged conditions with respect to unfaulty state.

When a fault occurs, the transfer functions of the affected components change, and the related logic sequences, updated with the use of isolated sub-models, are shown in Fig. 3-ii and Fig. 3-iii, for fault f_1 and fault f_2 , respectively. The logical connections derived from the use of isolated sub-models are highlighted with light edges, whereas the conditions unchanged with respect to the unfaulty state are sketched with dotted edges. According to these new sequences, the residuals related to the complete model (i.e. equation (1)) still diverge from 0 for both faults, whereas those expressed in equation (2) show a specific pattern for each faulty event, as summarized in the FSM of Table 3. Through this new FSM, a univocal isolation of the considered faults can be achieved, since all fault signatures show their own pattern.

Table 3: Fault Signature Matrix based on the residuals computed in equations (1) and (2) and the logic sequences illustrated in Fig. 3.

Event	Symptom s_1	Symptom s_2	Symptom s_3	Symptom s_4	Symptom s_5	Symptom s_6
Fault f_1	1	1	1	1	1	0
Fault f_2	1	1	1	0	0	1

It is worth observing that, from a theoretical point of view, the FSM presented in Table 3 can be used also for multiple fault detection. Indeed, with respect to the proposed example, in case of both faults f_1 and f_2 take place at the same time, all the defined residuals diverge from their unfaulty behaviour, leading all the related

1 symptoms to be 1. Observing that this new pattern can be generated only by the occurrence of these two
2 faults combined together, multiple fault detection can be achieved. Nevertheless, the feature applies only for
3 the considered faults, without taking into account other unexpected events.
4
5

6 The proposed theoretical approach presented in this section is applied to an SOFC AOGR system, whose
7 features, detailed scheme and modelling representation has been already illustrated in [41]. The aim of the
8 following analysis is to prove the feasibility of the theoretical approach on a real system configuration.
9 Aiming at on-board implementation for on-field uses, the methodology is firstly analysed in an ideal case
10 study, and then a realistic scenario is addressed, highlighting the main limitations that can arise when
11 approaching the practical application of the methodology to a real system.
12
13
14
15
16
17
18

19 **4. SOFC AOGR system scheme and faults description**

20 The system considered in this work is the SOFC AOGR system described in [41] and experimentally
21 studied for diagnostic purposes in [42]. This system is made of a 10 kW SOFC stack with anode off-gas
22 recycling unit, as shown in the scheme proposed in Fig. 4, where the stack and auxiliary components are
23 sketched. At cathode side, an air blower provides the required oxygen to the stack, heated up through the air
24 heat exchanger before reaching the stack cathode inlet. At anode side, part of the anode exhaust is
25 recirculated through the AOGR blower and mixed with fresh methane, before being heated up through the
26 fuel heat exchanger and sent to the fuel reformer. At this stage, the proper conversion of methane in
27 hydrogen for the stack is achieved and the resulting fuel mixture is sent to the stack anode inlet. The exhaust
28 gases are burned into the afterburner and used to heat up the fresh air flow.
29
30
31
32
33
34
35
36
37
38
39
40
41

42 In the cited work [41], a lumped dynamic model of the SOFC stack was developed and identified against
43 experimental data. This model is here considered to reproduce stack performance, interacting with the other
44 auxiliary components. The reformer model has been taken from [48], whereas the other component models
45 have been adapted from [3]. The scheme proposed in Fig. 4 also illustrates the different gas streams flowing
46 through the system (i.e. air, fuel and exhausts), as well as the sensors considered for the performance
47 evaluation of the diagnostic approach introduced in Section 3.2.
48
49
50
51
52
53
54

55 As described in [41] and [42], a stack leakage was identified by examining measured and simulated gas
56 compositions at stack outlet. This analysis has been carried out in laboratory environment and proved valid
57 through detailed physical modelling investigation. However, the use of gas composition measurements is
58
59
60
61
62
63
64
65

quite unfeasible when addressing on-field applications, due to both cost and installation issues. Therefore, their utilization in practical diagnostic applications for such systems cannot be considered, with consequent reduction in diagnostic efficacy (i.e. correct fault detection and isolation may be hindered).

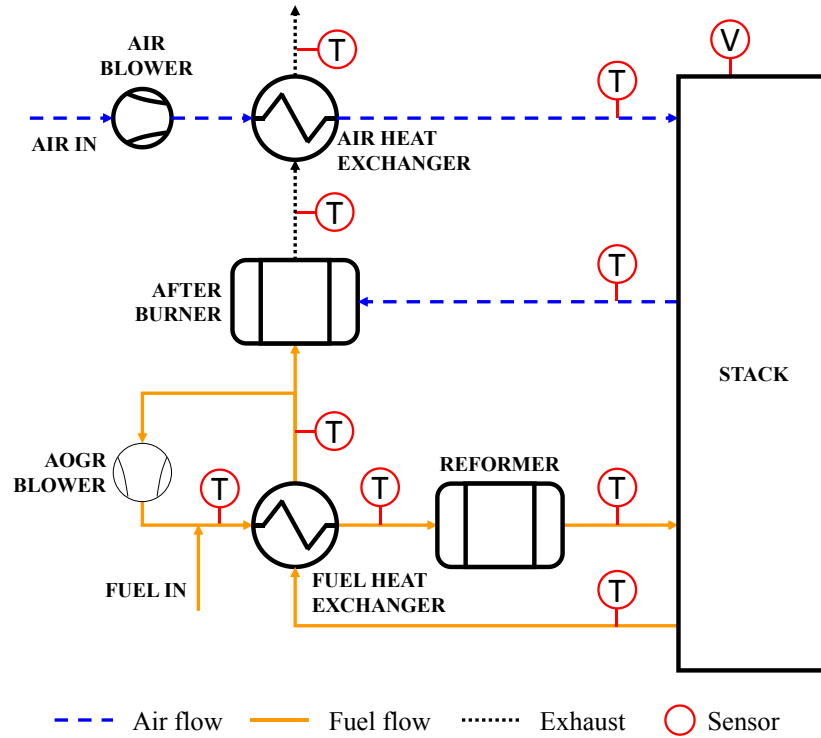


Fig. 4: SOFC AOGF system scheme with SOFC stack and six auxiliary components: air and AOGF

blowers, air and fuel heat exchangers, reformer and afterburner; air, fuel and exhaust flows as well sensors (i.e. monitored variables) considered for fault diagnosis are sketched.

Under this assumption, the diagnostic methodology presented in this paper is customized on the considered SOFC AOGF system, without involving measured gas compositions as features for diagnosis. The algorithm is tested with respect to the faults listed in Table 4, whose description is given in the following with an insight into their energetic impact on the affected components.

4.1 Faults description and energetic analysis

The faults here addressed have been chosen in accordance with system manufacturers experience, as among the most likely to happen and of a certain relevance for algorithm performance understanding and test. As per example, hydrogen leakage from the stack can induce fast performance decay if not properly

detected and isolated. As previously remarked, this fault has been already investigated in other works [41][42], and is here accounted for as stack fault. The remaining faults refer to other system components, mainly aiming at demonstrating the capability of the algorithm to perform proper diagnosis at whole system level. It is worth remarking that such list is essentially introduced for algorithm testing purposes and it can be easily enlarged to account for other faults of interest.

Table 4: Considered faults with brief description.

Fault	Description
f_1	Hydrogen external leakage from SOFC stack
f_2	Fuel heat exchanger efficiency loss
f_3	Air heat exchanger efficiency loss
f_4	AOGR blower malfunction

4.1.1 Stack fault: hydrogen leakage

The first fault f_1 is associated to a hydrogen external leakage from the SOFC stack to the surroundings due to, e.g., natural hydrogen diffusion through stack components or partial sealing degradation [42]. Being hydrogen the lightest and smallest component of the inlet fuel mixture, it is here assumed that part of the hydrogen provided by the reformer to the stack does not reach the reaction sites and leaves the whole system unreacted.

From an energetic point of view, this leakage induces a reduction in the energy available for the electrochemical reactions, affecting both electrical and thermal power output of the stack. It is worth bearing in mind that such system generally operates with fuel utilization lower than one (i.e. more fuel is provided with respect to the stoichiometry); therefore, the leakage may not affect the stoichiometric reaction rate and, thus, the requested current production. However, the stack voltage is affected in any case, since the inlet hydrogen partial pressure (influencing the ideal Nernst potential [49]) reduces, changing the compositions

1 and energy content of the gas mixture. Consequently, both anode and cathode outlet temperatures and gas
2 compositions decrease with respect to unfaulty conditions.
3

4 These changes directly affect the fuel heat exchanger. This component receives at hot inlet a smaller flow
5 amount at lower temperature. Therefore, despite behaving normally, less heat is exchanged from hot to cold
6 side, inducing a reduction in both hot and cold outlet temperatures. At this stage, the AOGR blower
7 recirculates an unchanged flow value with respect to normal state, but with a different composition and a
8 lower temperature. Accordingly, the mixing with fresh inlet methane (FUEL IN arrow in Fig. 4) induces a
9 reduction in the outlet blower temperature, which implies a decrease in the inlet temperature at the cold side
10 of the fuel heat exchanger, and a further decrease in its outlet temperatures.
11
12
13
14
15
16
17
18

19 As additional consequence, the pre-reformer receives an inlet gas mixture with a different hydrogen
20 composition (due to recirculation) and a lower temperature with respect to unfaulty system operation. This
21 induces a variation in the reforming process, with a direct change in the reaction temperature and outlet gas
22 composition. In parallel, the afterburner receives, from both fuel heat exchanger and cathode outlet, gas
23 flows with changed composition and temperature, inducing a decrease in the inlet energy amount and a
24 consequent reduction in the outlet temperature. In turn, the air heat exchanger takes at hot inlet less energy to
25 be exchanged with the cold inlet, decreasing the outlet temperatures and, thus, that of cathode inlet.
26
27
28
29
30
31
32
33
34

35 All these changes in cascade furtherly influence stack inlet compositions and temperatures, with an
36 amplification in the overall fault effects.
37
38
39

40 *4.1.2 Fuel heat exchanger fault: loss in exchange efficiency*

41

42 Fault f_2 addresses a reduction in the exchange efficiency of the fuel heat exchanger. This event can be
43 caused, for instance, by exchange surface fouling due to corrosion/erosion or material deposition [3][8]. Such
44 fault prevents part of the heat owned by hot inlet fluid to be transferred to cold fluid. This implies a higher
45 outlet temperature at hot side and a lower outlet temperature at cold side, with respect to unfaulty conditions.
46
47
48
49
50

51 On the one hand, the decrease in the cold outlet temperature of the fuel heat exchanger directly affects the
52 fuel pre-reformer, which receives a gas mixture with a reduced energy content. This induces a change in the
53 reforming process, and, in turn, a decrease in the reaction temperature and a variation in the outlet gas
54 composition. On the other hand, the rise in the hot outlet temperature of the fuel heat exchanger leads to an
55 increase in the energy content at both AOGR blower and afterburner inlets, with a consequent grow in their
56
57
58
59
60
61
62
63
64
65

1 outlet temperatures. Therefore, the hot inlet of the air heat exchanger presents a higher energy content, which
2 increases its outlet temperatures.
3

4 The stack behaviour may not be easily characterized since two opposite effects take place: the anode inlet
5 temperature decreases, whereas the cathode inlet temperature increases. The net change in stack outlet
6 temperature and, thus, stack voltage is a trade-off between the two inlet conditions: they could either
7 increase or decrease (or remain almost unchanged).
8
9

10 *4.1.3 Air heat exchanger fault: loss in exchange efficiency*

11 Similar comments made for the previous fault can be done for fault f_3 , which entails the loss in exchange
12 efficiency of the heat exchanger located at air side. This fault induces a reduction in the heat transferred from
13 hot to cold fluid, thus lowering, on the one hand, the cold outlet temperature, and increasing, on the other
14 hand, the hot outlet one. This event results in a decrease in the energy content (i.e. temperature) at cathode
15 inlet, with a consequent reduction in outlet stack temperatures and voltage. Therefore, all the components
16 connected to the stack are affected and their inlet energy content decreases. As a direct consequence, the
17 whole system exhibits a reduction in all components outlet temperatures, particularly at the afterburner
18 outlet. This latter implies a decrease in the hot inlet temperature at air heat exchanger, with a further
19 strengthening of the fault effects.
20
21
22
23
24
25
26
27
28
29
30
31
32
33
34

35 *4.1.4 AOGR blower fault: malfunction*

36 The last fault f_4 entails a malfunction in the AOGR blower, due to, for example, an increase in motor
37 friction or blower motor actuator error [3]. This malfunction leads to a reduction in the recirculated flow,
38 with less fuel reaching the reformer inlet and, thus, the stack. However, the un-recirculated fuel fraction is
39 sent to the afterburner, thus increasing its inlet energy content. This clearly implies an increase in afterburner
40 outlet temperature, with a consequent growth in the outlet temperatures of the air heat exchanger. This latter
41 event induces an increase in cathode inlet temperature, with an overall rise of the stack outlet temperatures
42 and voltage. Therefore, the fuel heat exchanger receives more energy at the hot inlet side, with a
43 straightforward increase in both hot and cold outlet temperatures. Moreover, this latter occurrence provides
44 the AOGR blower with higher inlet temperature, thus rising its outlet one.
45
46
47
48
49
50
51
52
53
54
55
56

57 All the faults here described are implemented in a complete system model, so as to reproduce their effects
58 in a simulated environment, as well as to perform a preliminary test of the proposed diagnostic algorithm.
59
60
61
62
63
64
65

1 This analysis represents a first assessment of the algorithm performance. The use of a simulated environment
2 gives the possibility to investigate under a wider range of cases the main advantages and drawbacks of the
3 algorithm, which may not be observed by means of real experimental test bench due to, e.g., unknown fault
4 magnitude, unfeasibility of inducing certain faults in a safe way, occurrence of undesired phenomena or
5 system failure.
6
7
8
9

10 In the next section, the results obtained through the simulation analysis of the algorithm are presented and
11 discussed. The algorithm is initially tested in an ideal case scenario, with a qualitative analysis of residual
12 deviations to investigate the theoretical fault isolability that can be achieved (as done in the example
13 described in Section 3.2.2). Then, a realistic scenario is addresses, introducing a quantitative evaluation of
14 residual changes and discussing the practical issues to be faced for the application of the methodology on
15 real systems.
16
17
18
19
20
21
22
23

24 **5. Fault diagnosis results and discussion**

25 As described in the previous section, the SOFC AOCR system model used in this paper derives from the
26 works [3], [41] and [48]. This model is here used as virtual test bench to simulate the whole system in both
27 faulty and unfaulty conditions. As illustrated in Fig. 5, three different simulation blocks, namely *system*,
28 *complete model* and *isolated sub-models*, are considered. The first block embeds the faulty version of the
29 whole system model, where specific equations are implemented to emulate the real system affected by the
30 faults listed in Table 4 (same role of the *system* block in Fig. 1-a). The second block embeds the unfaulty
31 version of the whole system model, to emulate the role of the model implemented in the diagnostic algorithm
32 (same role of the *complete model* block in Fig. 1-b). The third block embeds all system component sub-
33 models, fed with variables coming from the *system* block (same role of the *isolated sub-models* block in Fig.
34 1-c).
35
36
37
38
39
40
41
42
43
44
45
46
47
48

49 The physical variables accounted for residuals computation are chosen in accordance with the sensors
50 sketched in Fig.4. Clearly, any variable coming from the *system* block has two corresponding simulated
51 variables, one coming from the *complete model* block and another one from the *isolated sub-model* block.
52 Therefore, each variable leads to the computation of two different residuals and, in turn, to the definition of
53 two distinct analytical symptoms. This condition ensures the increase in redundancy information with respect
54 to a conventional diagnostic approach, where only the use of the *complete model* block would be conceived.
55
56
57
58
59
60
61
62
63
64
65

The list of the considered physical variables is given in Table 5, with the corresponding symptoms number related to the use of *complete model* and *isolated sub-models* blocks. This numbering is as well recalled in the scheme sketched in Fig. 5.

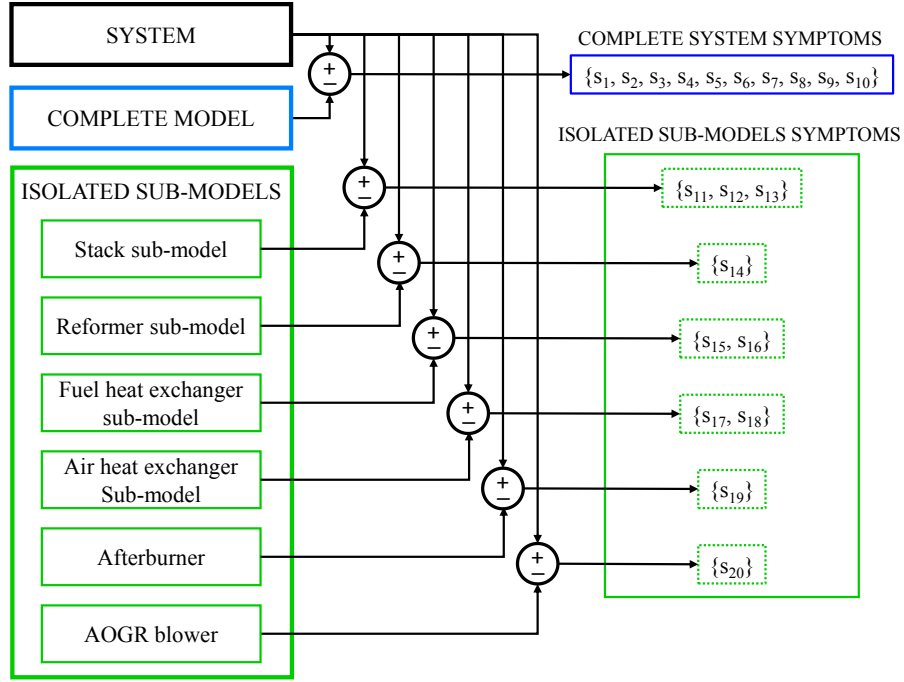


Fig. 5. Simulation blocks and related symptoms, with numbering linked to the variables listed in Table 5.

5.1 Ideal case: sub-model inputs totally provided by faulty system model

A first assessment of the diagnostic methodology is performed considering an ideal case scenario, where the *system* block model provides all the necessary inputs to the isolated system components sub-models. In this case, according to the theoretical analysis performed in Section 3.2.2, any residual computed through a sub-model corresponding to a component not affected by a fault do not deviate, and its related symptom is 0 (see Fig. 3 and Table 3). The residuals are evaluated as percentage deviations with respect to the unfaulty state, according to the following expression:

$$r = \frac{v_{\text{faulty}} - v_{\text{unfaulty}}}{v_{\text{unfaulty}}} \cdot 100 \quad (3)$$

where v_{faulty} represents a variable coming from the *system* block, whereas v_{unfaulty} is the corresponding variable simulated by either the *complete model* or the *isolated sub-models* block.

Table 5: Physical variables considered for residuals computation and related analytical symptoms, itemized with respect to the use of *complete model* or *isolated sub-models* blocks.

Monitored variable	Complete model	Isolated sub-models
Anode outlet temperature	S ₁	S ₁₁
Cathode outlet temperature	S ₂	S ₁₂
Stack voltage	S ₃	S ₁₃
Reformer outlet temperature	S ₄	S ₁₄
Fuel heat exchanger hot outlet temperature	S ₅	S ₁₅
Fuel heat exchanger cold outlet temperature	S ₆	S ₁₆
Air heat exchanger hot outlet temperature	S ₇	S ₁₇
Air heat exchanger cold outlet temperature	S ₈	S ₁₈
Afterburner outlet temperature	S ₉	S ₁₉
AOGR blower outlet temperature	S ₁₀	S ₂₀

The faults listed in Table 4 are simulated at four different magnitudes, that are 5%, 10%, 15% and 20%. These magnitudes are set assuming that a 0% magnitude means unfaulty state, whereas 100% magnitude refers to component/system failure [3]. Considering hydrogen external leakage (fault f_1), this fault is simulated by reducing the hydrogen molar flow at anode inlet by a certain amount. Therefore, a 5% magnitude for this fault means that the leaked amount of hydrogen leaving the stack towards the surroundings corresponds to 5% of the overall hydrogen flow at stack inlet. The remaining hydrogen flow reaching the anode reaction sites corresponds to the 95% of the unfaulty inlet amount. In case of heat

1 exchangers efficiency losses (faults f_2 and f_3), these faults are simulated by reducing the efficiency of the
2 concerned heat exchanger by a certain percentage. Hence, a 5% fault magnitude corresponds to a reduction
3 in the components efficiencies by 5% with respect to its unfaulty value. For the AOGR blower malfunction
4 (fault f_4), this last fault is simulated reducing the amount of recirculated fuel coming from the anode exhaust.
5
6 As the previous cases, a 5% magnitude means that the recirculated flow amount is reduced by 5% compared
7 to its unfaulty value. The same reasoning can be applied to all the other fault magnitudes.
8
9

10
11 The results in terms of residual deviations for all the considered faults are shown in Fig. 6 through Fig. 9.
12
13 The solid blue lines with circle markers refer to the residuals computed with the *complete model* block,
14
15 whereas the dashed green lines with square markers are related to those evaluated with the *isolated sub-*
16
17 *models* block. In each plot, the left y-axis is related to complete model residuals whereas the right y-axis to
18
19 sub-model residuals. Moreover, the symptoms numbering is consistent with that proposed in Table 5.
20
21
22

23
24 As preliminary comment, it can be observed that all the residuals evaluated by means of the *complete*
25
26 *model* block deviate from 0 in each case. This result proves the theoretical unfeasibility of isolating any of
27
28 the considered faults with the only use of the complete model: fault detection can be achieved, but fault
29
30 isolation is hindered, since all the related symptoms are theoretically triggered. The use of isolated sub-
31
32 models can solve this issue, as discussed below.
33
34

35
36 With respect to fault f_1 , whose results are presented in Fig. 6, all the residuals computed with the *complete*
37
38 *model* block are negative. This means that each faulty variable is lower than the related unfaulty one (see
39
40 equation (3)). This result is perfectly in accordance with the fault effects described in section 4.1.1.
41
42 Observing the residuals computed with the *isolated sub-models* block, only three of them deviate from 0 at
43
44 any fault magnitude, that are anode outlet temperature (symptom s_{11}), cathode outlet temperature (symptom
45
46 s_{12}) and stack voltage (symptom s_{13}). These residuals are all related to the stack sub-model, which refers to
47
48 the only component under fault, confirming the theoretical assumption introduced in Section 3.2.
49
50 Temperature residuals are both positive, whereas voltage residual is negative. This result can be explained
51
52 considering that the isolated stack sub-model does not suffer from hydrogen leakage, and the deviations from
53
54 the unfaulty conditions are only due to the faulty inputs provided by the *system* block. This means that all the
55
56 inlet hydrogen flow is kept within the stack, ensuring a greater hydrogen partial pressure and a voltage
57
58 higher than that of the faulty system (explaining the negative residual). This induces an increase in the
59
60
61
62
63
64
65

generated electric power and a reduction in the thermal power, with a consequent decrease in both cathode and anode outlet temperatures with respect to the faulty state (explaining the positive residual trends).

It is worth observing that the deviation of the isolated sub-model residuals is quite small, implying that the values coming from the *system* block do not differ much from those of the *isolated sub-model* block. This result highlights that the fault itself does not have a strong direct influence on stack behaviour, but its effects are instead amplified by the other system components (as already commented at the end of Section 4.1.1).

Concerning fault f_2 , its simulation results are shown in Fig. 7. The deviation of the residuals computed by means of the *complete model* block is in accordance with the faults effects illustrated in Section 4.1.2. It can be observed that stack residuals (i.e. symptoms s_1 , s_2 and s_3) show a small deviation, due to the trade-off between anode inlet temperature decrease and cathode inlet temperature increase.

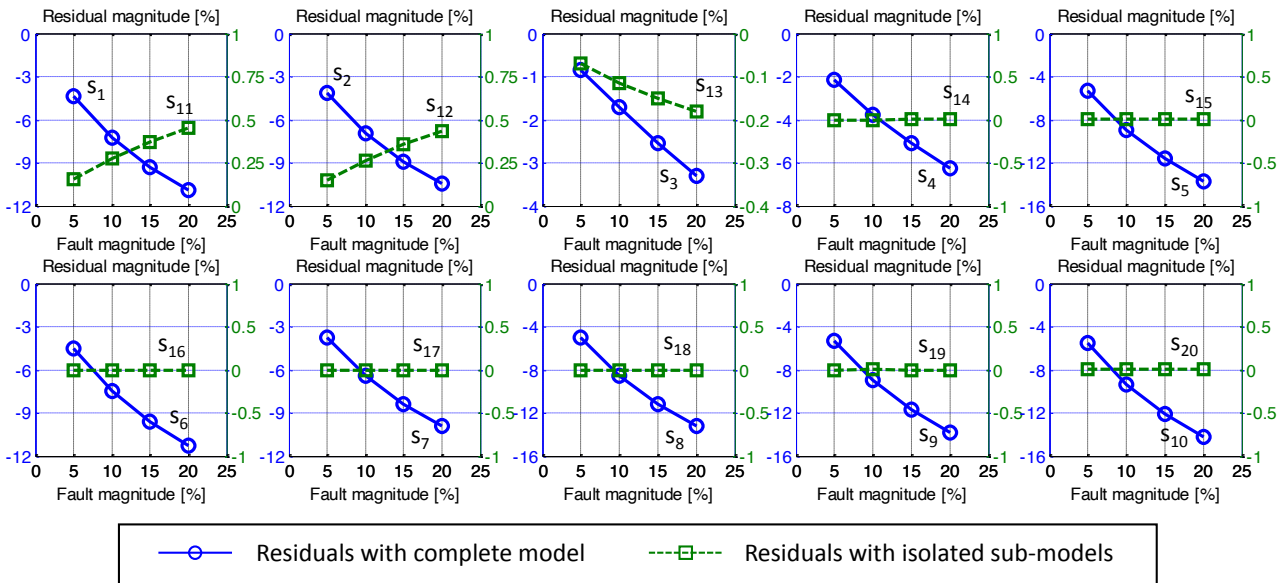


Fig. 6. Fault f_1 (stack): residuals obtained with complete system model (solid blue line and circle marker) and isolated sub-models (dashed green line and square marker); the left y-axis is related to complete model residuals whereas the right y-axis to sub-model residuals.

Analysing the residuals computed with the isolated sub-models, only those related to fuel heat exchanger hot and cold outlet temperatures (symptoms s_{15} and s_{16} , respectively) are different from 0 at any fault magnitude. The former residual is positive, whereas the latter negative. This is due to the higher energy amount exchanged by hot and cold flow in the isolated sub-model, since its efficiency is not affected by the

1
2
3
4
5
6
7
8
9
10
11
12
13
14
15
16
17
18
19
20
21
22
23
24
25
26
27
28
29
30
31
32
33
34
35
36
37
38
39
40
41
42
43
44
45
46
47
48
49
50
51
52
53
54
55
56
57
58
59
60
61
62
63
64
65

fault. This causes the hot outlet temperature of the sub-models to be lower than that computed with the faulty system, whereas the cold outlet temperature to be higher.

Similar observations made for the previous fault can also be done for fault f_3 , whose results are shown in Fig. 8. Again, all the residuals computed with the *complete model* block change according to the fault effects described in Section 4.1.3. An interesting comment can be done on the residual related to the hot outlet temperature of the air heat exchanger (symptom s_7): this residual is first negative and then positive. This expresses the initial temperature reduction due to the decrease in hot inlet temperature coming from the afterburner, but then the variation in the exchanged heat compensates this effect, thus causing the hot outlet temperature to rise.

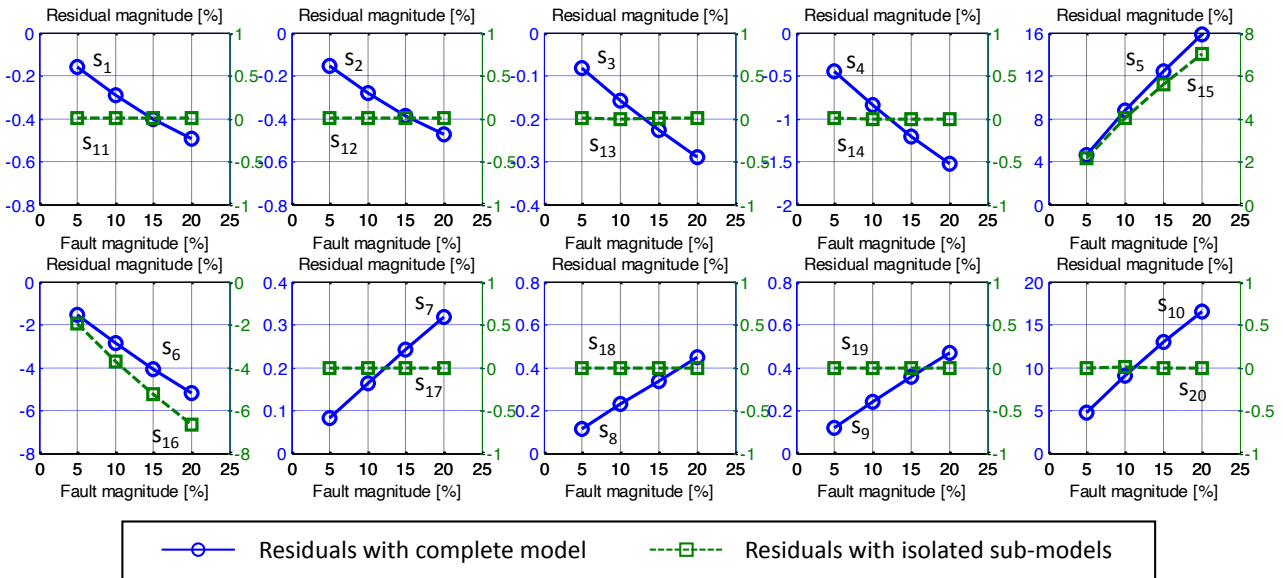


Fig. 7. Fault f_2 (fuel heat exchanger): residuals obtained with complete system model (solid blue line and circle marker) and isolated sub-models (dashed green line and square marker); the left y-axis is related to complete model residuals whereas the right y-axis to sub-model residuals.

Analysing the residuals computed with the isolated sub-models, only those related to the air heat exchanger hot and cold outlet temperatures (symptoms s_{17} and s_{18} , respectively) are different from 0 at any fault magnitude, being positive the former and negative the latter. Also in this case, the reason lies in the higher energy amount exchanged by hot and cold flow in the sub-model, leading outlet hot temperature to be lower and cold outlet temperature to be higher compared to the faulty system ones.

The results concerning AOGR blower fault f_4 are presented in Fig. 10. In accordance with the energetic analysis of the fault effects, all the residuals show a positive trend. Indeed, as explained in Section 4.1.4, this fault induces an increase in the whole system temperature (i.e. at each component outlet). The negative effect can be observed in the fuel utilization, since less fuel is recirculated and thus involved in the electrochemical reaction; nevertheless, such an effect negatively impacts on the efficiency of the whole system. On the other hand, observing the residuals computed with isolated sub-models, the only one changing is that of the AOGR blower (symptom s_{20}), particularly showing a negative trend. This behaviour is motivated by considering that the temperature simulated with the sub-model at the AOGR outlet (right before mixing with fresh methane) is higher than that of the faulty system. Therefore, the reason is related to the higher temperature at AOGR inlet, which leads to an increase in the energy content at the mixing junction and thus the temperature.

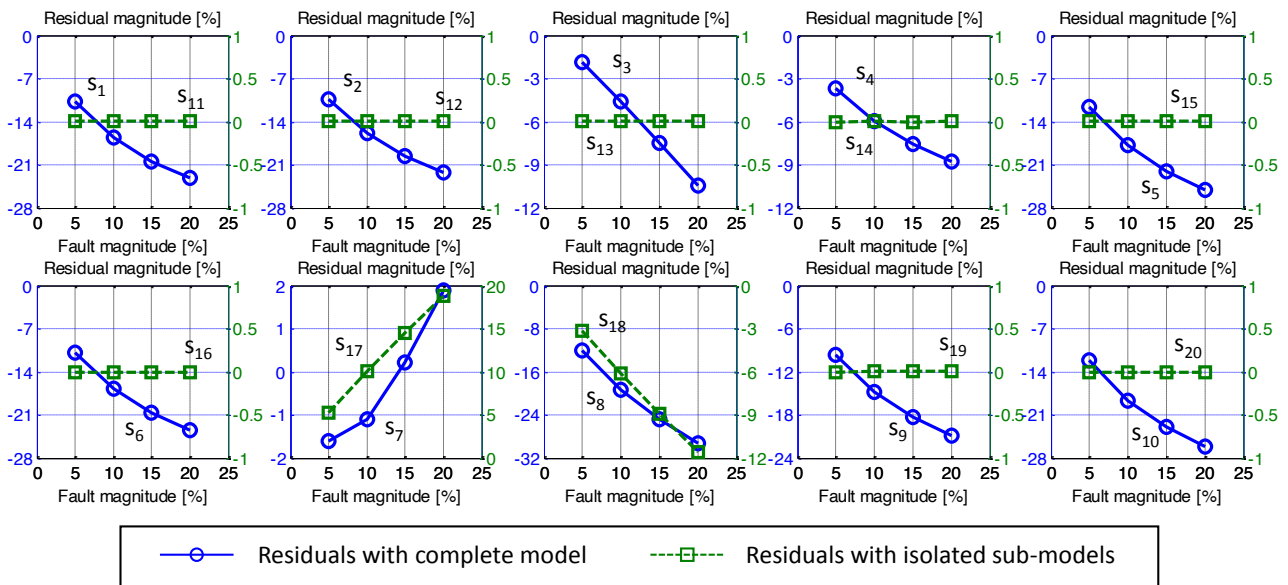


Fig. 8. Fault f_3 (air heat exchanger): residuals obtained with complete system model (solid blue line and circle marker) and isolated sub-models (dashed green line and square marker); the left y-axis is related to complete model residuals, whereas the right y-axis to sub-model residuals.

1
2
3
4
5
6
7
8
9
10
11
12
13
14
15
16
17
18
19
20
21
22
23
24
25
26
27
28
29
30
31
32
33
34
35
36
37
38
39
40
41
42
43
44
45
46
47
48
49
50
51
52
53
54
55
56
57
58
59
60
61
62
63
64
65

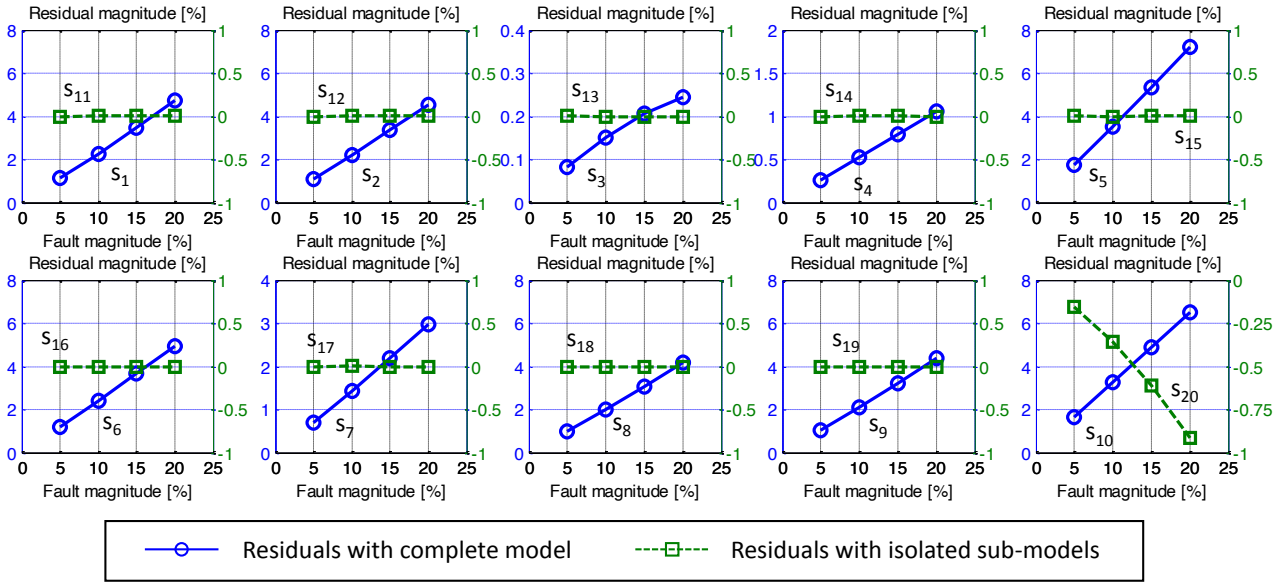


Fig. 9. Fault f_4 (AOGR blower): residuals obtained with complete system model (solid blue line and circle marker) and isolated sub-models (dashed green line and square marker); the left y-axis is related to complete model residuals, whereas the right y-axis to sub-model residuals.

The illustrated results can be summarized through the theoretical FSM presented in Table 6. It is worth remarking that this FSM takes into account only the existence of a residual deviation from 0, without considering its quantitative drift. The analysis of the faults patterns confirms the advantage of using isolated sub-models for fault isolation. Indeed, considering just the symptoms available with the *complete model* block, univocal fault isolation is totally hindered for all the considered faults, since the first ten symptoms are all 1. Hence, the introduction of the symptoms generated with the *isolated sub-models* block ensure complete univocal fault isolation, leading the rows of the whole FSM to be different from one another.

A first step concerning the practical implementation of the proposed algorithm consists in taking into account the actual effects of the considered faults on the generated residuals. Indeed, in real applications, residuals are affected by noise and model uncertainties; thus, they can be different from 0 even during unfaulty conditions (when they should be theoretically 0). This consideration implies the introduction of proper threshold levels for symptoms generation (as commented in Section 3.1 and thoroughly described in [3]). Nevertheless, during faulty states, although different from 0, some residuals may deviate much less than expected (depending on fault magnitude and variable sensitivity to the fault) and they could not overcome the thresholds. Thus, a real symptoms pattern of a fault can substantially differ from its theoretical one.

Table 6: Theoretical FSM related to the SOFC AGR system for the fault simulation results presented in Fig. 6 through Fig. 9.

Event	Symptoms from complete mode										Symptoms from isolated sub-models									
	s_1	s_2	s_3	s_4	s_5	s_6	s_7	s_8	s_9	s_{10}	s_{11}	s_{12}	s_{13}	s_{14}	s_{15}	s_{16}	s_{17}	s_{18}	s_{19}	s_{20}
f_1	1	1	1	1	1	1	1	1	1	1	1	1	1	0	0	0	0	0	0	0
f_2	1	1	1	1	1	1	1	1	1	1	0	0	0	0	1	1	0	0	0	0
f_3	1	1	1	1	1	1	1	1	1	1	0	0	0	0	0	0	1	1	0	0
f_4	1	1	1	1	1	1	1	1	1	1	0	0	0	0	0	0	0	0	0	1

For this reason, a quantitative evaluation of residuals deviation should be performed, to address practical application of the diagnostic algorithm. In this case, the achieved FSM is characterized on fault magnitude and specific threshold levels. For instance, for all the residuals shown in Fig. 6 through 9, a fault magnitude of 10% is considered and a detection threshold range of $\pm 1\%$ is defined (as also done in [3]). At this fault magnitude, any residual value greater than +1%, or lower than -1%, causes the related symptom to be 1, thus leading to the FSM presented in Table 7. With respect to the theoretical FSM of Table 6, it can immediately be observed that more symptoms are zeroed. Focusing on the first ten symptoms, the only use of the complete model leads now to improved fault isolability, but still two faults (faults f_1 and f_3) present the same pattern. The introduction of isolated sub-models symptoms allows fulfilling univocal fault isolation also under quantitative residual deviation analysis, leading to two different patterns for faults f_1 and f_3 .

Table 7: FSM based on the results presented in Fig. 6 through Fig. 9 considering a fault magnitude of 10% and setting a detection threshold range of $\pm 1\%$.

	Symptoms from complete mode										Symptoms from isolated sub-models									
Event	s ₁	s ₂	s ₃	s ₄	s ₅	s ₆	s ₇	s ₈	s ₉	s ₁₀	s ₁₁	s ₁₂	s ₁₃	s ₁₄	s ₁₅	s ₁₆	s ₁₇	s ₁₈	s ₁₉	s ₂₀
f_1	1	1	1	1	1	1	1	1	1	1	0	0	0	0	0	0	0	0	0	0
f_2	0	0	0	0	1	1	0	0	0	1	0	0	0	0	1	1	0	0	0	0
f_3	1	1	1	1	1	1	1	1	1	1	0	0	0	0	0	0	1	1	0	0
f_4	1	1	0	0	1	1	1	1	1	1	0	0	0	0	0	0	0	0	0	0

5.2 Real case: sub-models fed by faulty and complete system models

The results presented in the previous section apply only if the *isolated sub-models* block is entirely fed by the *system* block. However, another major issue that should be taken into consideration, when dealing with practical application of the diagnostic algorithm, is that some inputs required by the sub-models cannot be provided by the system, due to, e.g., measurements unavailability or unfeasibility (such as gas composition measurements for on-field applications). Therefore, these remaining inputs must be provided by the *complete model* block. This condition leads to a mix of inputs supplied to the sub-models: some of them will be provided by the system (which operates in faulty conditions), whereas others by the complete model (which simulates unfaulty states). In such a case, the sub-models outputs will experience only a partial influence from the faults, since only part of the inputs will be in faulty state. Consequently, these outputs will be equal neither to faulty system outputs nor to complete model outputs.

A schematic representation of the difference between real case and ideal case scenarios is proposed in Fig. 10. The ideal case is illustrated in Fig. 10-a, where the sub-model receives all the inputs from the *system* block: sub-model output y'' will be equal to system component output y if the component is unfaulty. In the real case scenario (Fig. 10-b), the sub-model is fed by both *system* and *complete model* block: its output y''

will be different from both system output y and complete model output y' , also when the related system component is unfaulty.

With respect to the ideal case scenario illustrated in the previous section, the change in faults isolability is now investigated providing the *isolated sub-models* with *system* block variables only related to the sensors measurement sketched in Fig. 4 and listed in Table 5. The *complete model* block provides all the other required inputs (Fig. 10-b). The use of only such sensors (i.e. temperature and voltage) is considered a worst-case scenario, when mass flow and gas concentration measurements are not available. It is clear that, the increase in installed sensors (e.g. flow, pressure, etc.) can improve fault isolation, but fault clustering issues may still occur. Therefore, the use of the proposed methodology remains valid, although a case-by-case evaluation of the effectiveness could be done. Nonetheless, it is worth remarking that the increase in redundancy information (i.e., the symptoms number) is always a benefit for fault detection and isolation scopes [45].

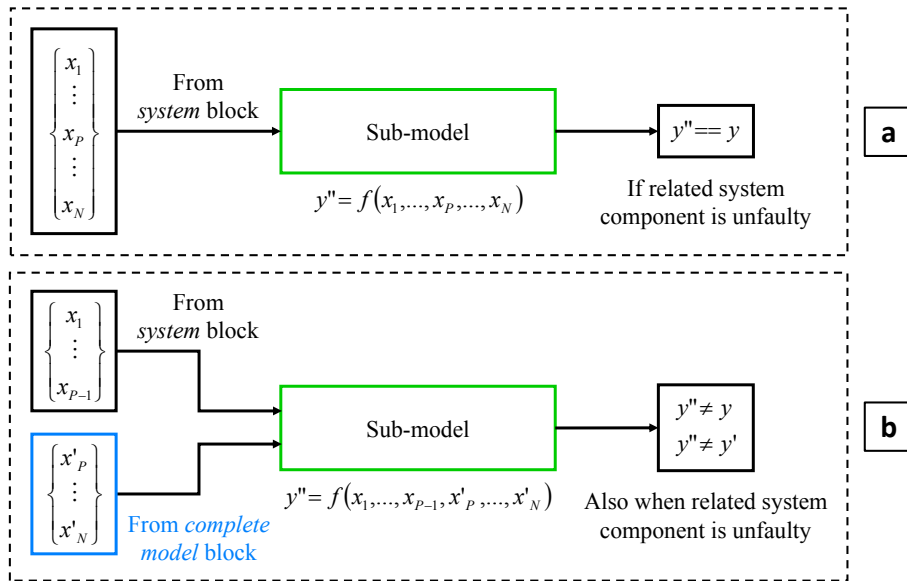


Fig. 10. Sub-model output response in case of inputs totally fed by *system* block (a) or partially provided by *complete model* block (b), with y , y' and y'' being *system* block, *complete model* block and *isolated sub-models* block outputs, respectively.

Also in this scenario, the study is performed simulating the faults listed in Table 4 and computing the residuals by means of equation (3). The simulation results are presented in Fig. 11 through Fig. 14. Clearly,

the residuals computed with the *complete model* block do not change, and they are not illustrated in the provided figures. To better appreciate the change in sub-model residuals trend, the new residuals, presented in each plot with a dot-dashed line and triangle marker, are compared with those evaluated in the ideal case scenario, still sketched with dashed green line and square marker (as done in Fig. 6 through Fig. 9).

Concerning fault f_1 (stack) (see Fig. 11), all the isolated sub-models are provided with faulty inlet temperatures and unfaulty inlet gas compositions. This means that all the isolated sub-models present the same inlet temperatures of the *system* block components. As expected, more residuals deviate from zero with respect to the ideal case scenario. Observing stack residuals (i.e. symptoms s_{11} through s_{13}), they show an opposite trend compared to the previous case. This behaviour can be explained considering that, given the same inlet temperatures, the isolated sub-models receive an inlet fuel flow with a greater hydrogen content (i.e. unfaulty), thus inducing an increase in the thermal energy produced by the reaction. Therefore, isolated sub-model outlet temperatures are higher than those of the faulty system, thus implying negative residuals (see equation (3)). The greater hydrogen content leads also the stack voltage to increase, with a consequent negative residual.

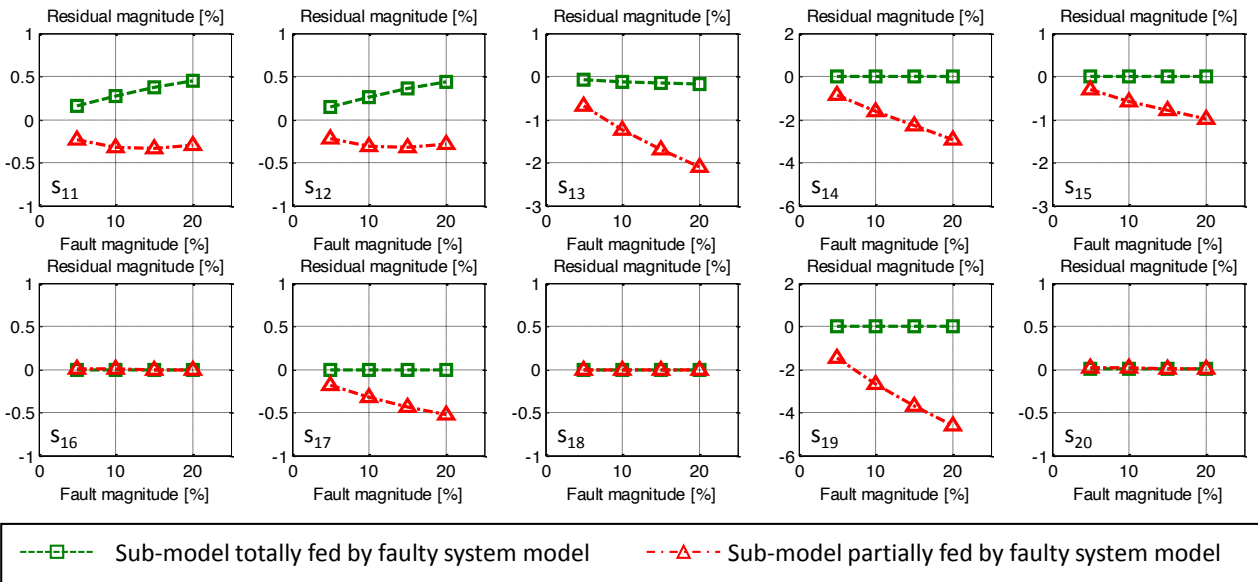


Fig. 11. Sub-model residuals for fault f_1 (stack) with different input feed: inputs fully provided by faulty system model (see scheme of Fig. 10-a) are sketched with dashed green lines and square markers as in Fig. 6; inputs provided by both faulty and nominal system models (see scheme of Fig. 10-b) are instead sketched with dot-dashed red lines and triangle markers.

1 The same reasoning considered for stack residuals can be applied to reformer and afterburner. Indeed,
2 their isolated sub-models show higher outlet temperatures (symptoms s_{14} and s_{19} , respectively) compared to
3 those of the system components. Once more, this is due to the greater hydrogen content, while keeping inlet
4 temperatures unchanged with respect to the faulty system.
5
6

7
8 A different explanation is instead given for heat exchanger sub-models residuals. Only hot outlet
9 temperatures (symptom s_{15} and s_{17}) are affected, whereas cold outlet temperatures (symptom s_{16} and s_{18})
10 remain unchanged (i.e. their residuals are 0). This effect can be justified considering that both hot and cold
11 inlet temperatures as well as cold inlet flow are the same with respect to the faulty state, whereas only the hot
12 inlet flow is higher. This implies a rise in the outlet energy content at hot side, while keeping unchanged the
13 energy transferred to the cold side, and consequently the outlet temperature. Also the AOGR blower outlet
14 temperature (symptom s_{20}) does not change, leading its residual to be 0 at any fault magnitude. This can be
15 expected since the recirculated flow amount remains the same (i.e. the blower do not experience any fault),
16 and the inlet temperature is that of the faulty system, thus leading to the same outlet temperature.
17
18
19
20
21
22
23
24
25
26
27

28 The results related to fault f_2 (fuel heat exchanger) are presented in Fig. 12. It is worth recalling from
29 Section 4.1.2 that, with respect to unfaulty conditions, this fault induces a change in the components outlet
30 temperatures and gas mixture compositions, while leaving unchanged the whole fuel flow amount.
31 Therefore, the isolated sub-models operate with the same inlet temperatures and overall inlet flows of the
32 faulty system components, resulting in an equal behaviour of the related residuals. However, only those of
33 the stack show a different trend, since they are affected by gas composition variation. Indeed, this influence
34 the electrochemical reaction rates, overall thermal and electric energy generation and outlet mixture
35 composition.
36
37
38
39
40
41
42
43
44
45

46 With respect to fault f_3 (air heat exchanger), whose results are illustrated in Fig. 13, the introduction of
47 unfaulty inlet compositions brings a wider change in computed residuals. The only unchanged residuals are
48 those related to the air heat exchanger and to the cold outlet temperature of the fuel heat exchanger. Stack,
49 reformer and afterburner residuals modify their behaviour due to the change in gas compositions, in
50 similarity with what discussed for fault f_1 . The hot outlet temperature residual related to the fuel heat
51 exchanger increases because, while keeping the inlet temperature unchanged, both hot and cold fluid heat
52 capacities vary with the inlet gas compositions. Therefore, also the heat exchanged between hot and cold
53
54
55
56
57
58
59
60
61
62

fluids changes, with a consequent decrease in the hot outlet temperature of the isolated sub-model. On the other hand, the AOGR blower residual is lower than 0 since the isolated sub-model is fed with an unfaulty gas composition and faulty inlet temperature. Therefore, when mixing with the fresh methane, the overall fuel mixture presents a higher energy content and thus an increased temperature, with respect to the faulty system.

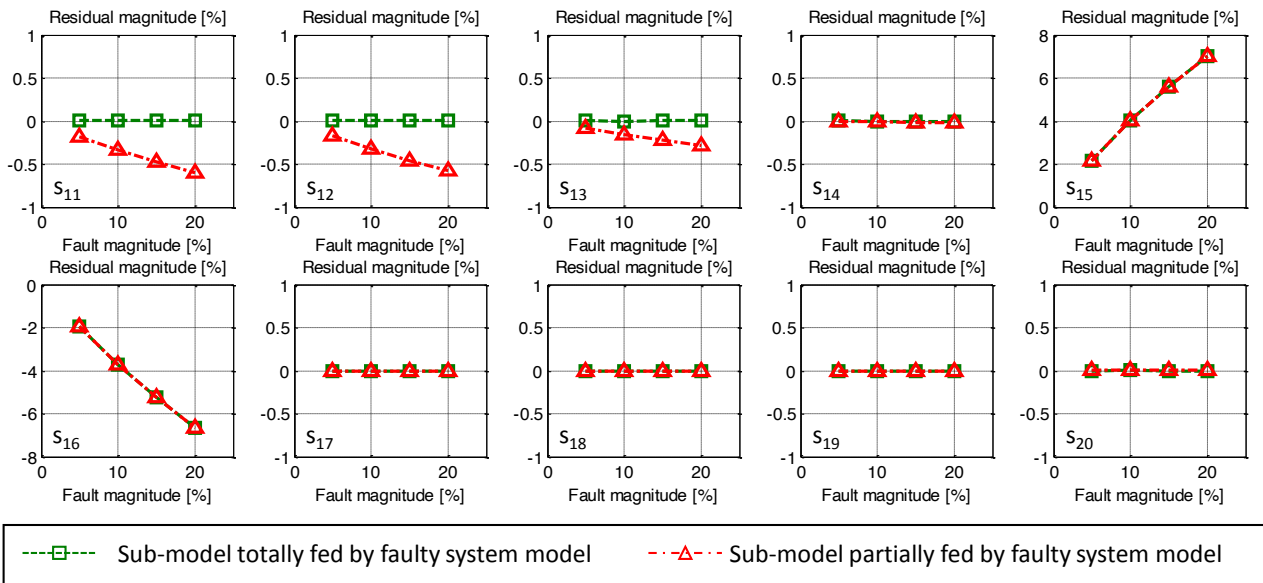


Fig. 12. Sub-model residuals for fault f_2 (fuel heat exchanger) with different input feed: inputs fully provided by the faulty system model (see scheme of Fig. 10-a) are sketched with dashed green lines and square markers as in Fig. 7; inputs provided by both faulty and nominal system models (see scheme of Fig. 10-b) are instead sketched with dot-dashed red lines and triangle markers.

Similar comments introduced for the previous cases can be also addressed for fault f_4 (AOGR blower) results, shown in Fig. 14. In this case, AOGR blower isolated sub-system is fed with inlet faulty temperature and unfaulty recirculated flow amount. This increases the energy content at the mixing point with fresh methane, rising sub-model outlet temperature, with respect to the faulty system. Analysing the stack residuals, they show a positive trend, meaning that the faulty system variables are higher than those of the isolated sub-model. This can be explained considering that the heat generated by the electrochemical reaction is distributed over a greater fuel amount recirculated by the AOGR blower, thus lowering both outlet temperatures and voltage.

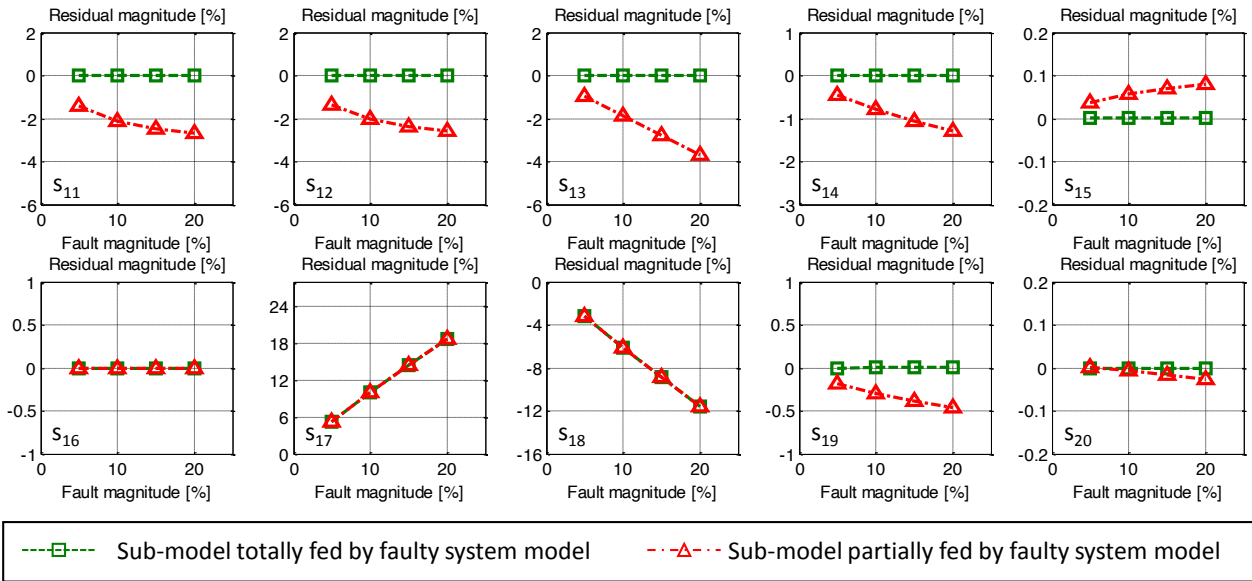


Fig. 13. Sub-model residuals for fault f_3 (air heat exchanger) with different input feed: inputs fully provided by the faulty system model (see scheme of Fig. 10-a) are sketched with dashed green lines and square markers as in Fig. 8; inputs provided by both faulty and nominal system models (see scheme of Fig. 10-b) are instead sketched with dot-dashed red lines and triangle markers.

With respect to the pre-reformer, the higher recirculation induces an increase in its outlet temperature, since more fuel is subject to the reforming process. Considering fuel heat exchanger residuals, the heat transferred from hot to cold side is distributed over a larger mass amount, since the recirculated flow is higher compared to faulty component. Therefore, while keeping the same cold outlet temperature, the hot outlet temperature decreases. The afterburner shows as well a decreased temperature, since less fuel burns with respect to faulty conditions.

The results presented in Fig. 11 through Fig. 14 are summarized in the FSM illustrated in Table 8. As done for the FSM of Table 7, this FSM is achieved considering a fault magnitude of 10% and a detection threshold range of $\pm 1\%$. Although provided with less measured variables (e.g. the use of faulty gas composition is avoided), the introduction of isolated sub-models still allows the univocal isolation of faults f_1 and f_3 , proving the robustness of the proposed approach also in real case scenario.

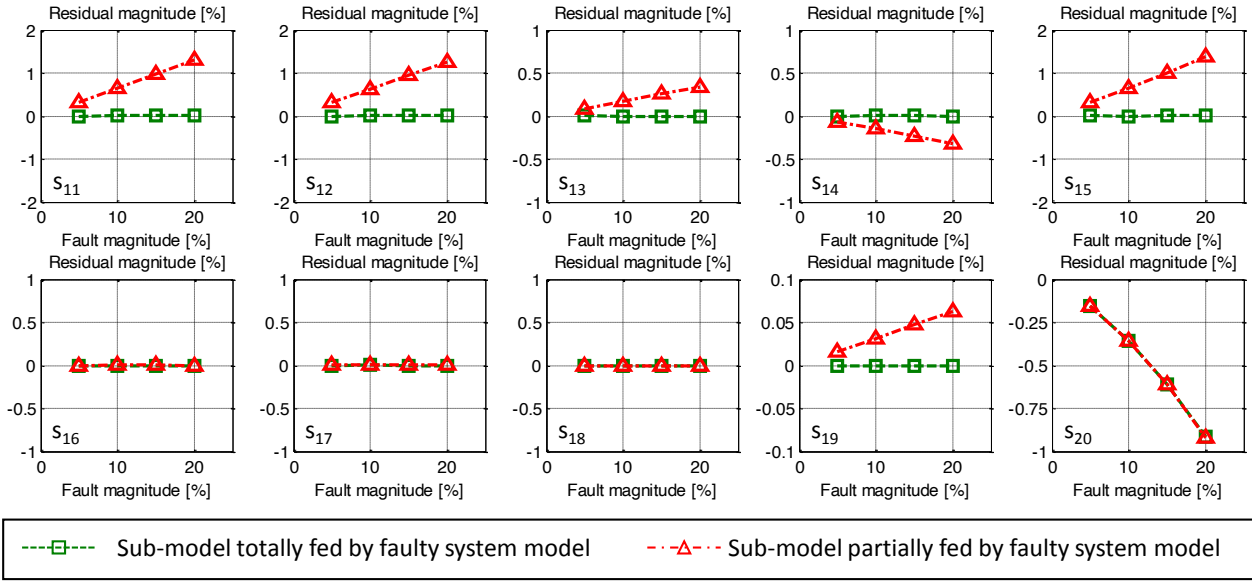


Fig. 14. Sub-model residuals for fault f_4 (AOGR blower) with different input feed: inputs fully provided by the faulty system model (see scheme of Fig. 10-a) are sketched with dashed green lines and square markers as in Fig. 9; inputs provided by both faulty and nominal system models (see scheme of Fig. 10-b) are instead sketched with dot-dashed red lines and triangle markers.

Table 8: Fault Signature Matrix based on the complete model residuals results presented in Fig. 6 through Fig. 9 and sub-model residuals (with inputs partially fed by both faulty and nominal models) presented in Fig. 11 through Fig. 14, considering a fault magnitude of 10% and setting a detection threshold range of $\pm 1\%$.

Event	Symptoms from complete model										Symptoms from isolated sub-models									
	s_1	s_2	s_3	s_4	s_5	s_6	s_7	s_8	s_9	s_{10}	s_{11}	s_{12}	s_{13}	s_{14}	s_{15}	s_{16}	s_{17}	s_{18}	s_{19}	s_{20}
f_1	1	1	1	1	1	1	1	1	1	1	0	0	1	1	0	0	0	0	1	0
f_2	0	0	0	0	1	1	0	0	0	1	0	0	0	0	1	1	0	0	0	0
f_3	1	1	1	1	1	1	1	1	1	1	1	1	1	0	0	0	1	1	0	0
f_4	1	1	0	0	1	1	1	1	1	1	0	0	0	0	0	0	0	0	0	0

6. Conclusions

The present paper described an innovative diagnostic technique based on component isolated sub-models analysis, which can solve fault isolation issues and achieve proper fault diagnosis of Solid Oxide Fuel Cell (SOFC) systems. The reduction in available on-board sensor measurements may induce fault clustering and thus hinder univocal fault isolation. According to the proposed approach, the use of isolated sub-models can increase residuals generation and thus improve suitable diagnostic information extraction.

The technique has been characterized and tested in simulated environment on an SOFC Anode Off-Gas Recycling (AOGR) system. Four different faults occurring at components level have been addressed, that are hydrogen external leakage, fuel and air heat exchangers efficiency reduction and recirculation unit malfunction. These faults have been implemented in a complete system model, used to simulate both nominal and faulty variables behaviours at four different magnitudes (i.e. 5%, 10%, 15% and 20%), defined with respect to unfaulty operating conditions.

From the ideal case scenario results, the residuals computed without the use of isolated sub-models showed the unfeasibility of fault isolation since all the residuals diverge from 0. Therefore, all the symptoms related to the complete model use, shown in the theoretical Fault Signature Matrix (FSM), are affected by all the considered faults (i.e. are all 1). The introduction of the isolated sub-models led to the definition of a set of symptoms only affected by specific faults, leading to univocal fault isolation and proving the theoretical correctness of the proposed approach also for complex systems.

To address the practical application of the proposed algorithm, a specific analysis has been then performed to assess the quantitative deviations of the residuals generated with both the complete model and the isolated sub-models. Percentage residuals behaviours are computed setting a fault magnitude of 10%. Then, a detection threshold range of $\pm 1\%$ has been considered, so as to perform fault detection. In this case, the achieved FSM showed two faults (i.e. hydrogen external leakage and air heat exchanger efficiency reduction) with the same pattern when using only the complete model residuals. Nevertheless, the introduction of isolated sub-model residuals solved fault isolability issue also with quantitative residuals analysis, leading to an FSM with univocal fault patterns. A further step towards practical algorithm use is performed considering that in a real case scenario the isolated sub-models are fed with inputs provided by both faulty system and complete model. This case represented actual system applications, when some

1
2
3
4
5
6
7
8
9
10
11
12
13
14
15
16
17
18
19
20
21
22
23
24
25
26
27
28
29
30
31
32
33
34
35
36
37
38
39
40
41
42
43
44
45
46
47
48
49
50
51
52
53
54
55
56
57
58
59
60
61
62
63
64
65

measurements (e.g. gas compositions) are not available for either cost or installation issues. Also in this case, the analysis has been performed simulating the faults at different magnitudes and checking the isolated sub-models residual deviation changes. Although more residuals diverge from nominal conditions, the introduction of isolated sub-model analysis still proved being significant for univocal fault isolation fulfilment.

The increase in fault diagnosis performance achievable with the use of the proposed technique can improve system operation, especially if a suitable interaction between diagnostic algorithm and system control strategy is defined. Indeed, specific adaptive control actions can be applied upon the knowledge of which fault is occurring in the system, to reduce maintenance need and thus lower system operation costs. Moreover, the proposed approach can be straightforwardly applied to other fuel cell technologies (e.g. Polymer Electrolyte Membrane, Direct Methanol, etc.) or systems (e.g. batteries, engines, etc.) if proper component models are available.

Acronyms

AOGR	Anode Off-Gas Recycling
APU	Auxiliary Power Unit
CHP	Combined Heat and Power
FTA	Fault Tree Analysis
FSM	Fault Signature Matrix
GT	Gas Turbine
LCA	Life Cycle Assessment
LNG	Liquid Natural Gas
RF	Random Forest
RNN	Recurrent Neural Network
RUL	Remaining Useful Life
SOEC	Solid Oxide Electrolyser Cell
SOFC	Solid Oxide Fuel Cell
SOM	Self Organization Map

SVM	Support Vector Machine
TCPG	Triple Combined-cycle Power Generation
VARs	Vapour Absorption Refrigerator System

Acknowledgements

The research leading to these results has received funding from the European Union's Seventh Framework Programme (FP7/2007-2013) for the Fuel Cells and Hydrogen Joint Technology Initiative under grant agreement n° 621208 (Project - DIAMOND, Diagnosis-aided control for SOFC power systems).

References

- [1] Singhal CS, Kendall K. High Temperature Solid Oxide Fuel Cells: Fundamentals, Design and Applications. Oxford, UK: Elsevier Ltd.; 2004.
- [2] Yan D, Zhang C, Liang L, Li K, Jia L, Pu J, et al. Degradation analysis and durability improvement for SOFC 1-cell stack. *Appl Energy* 2016;175:414–420.
- [3] Polverino P, Pianese C, Sorrentino M, Marra D. Model-based development of a fault signature matrix to improve solid oxide fuel cell systems on-site diagnosis. *J Power Sour* 2015;280:320–338.
- [4] Costamagna P, De Giorgi A, Magistri L, Moser G, Pellaco L, Trucco A. A Classification Approach for Model-Based Fault Diagnosis in Power Generation Systems Based on Solid Oxide Fuel Cells. *IEEE Trans Energy Convers* 2016;31:676–687.
- [5] Polverino P, Pianese C. Model-based prognostic algorithm for online RUL estimation of PEMFCs. SYSTOL16: Proceedings of the 3rd Conference on Control and Fault-Tolerant Systems; 2016 Sep 7–9; Barcelona, Spain.
- [6] Wu X, Ye Q. Fault diagnosis and prognostic of solid oxide fuel cells. *J Power Sour* 2016;321:47–56.
- [7] Terayama T, Momma A, Tanaka Y, Kato T. Efficiency Gain of Solid Oxide Fuel Cells by Using Anode Gas Recycle. *Electrochem Soc Trans* 2015;65:199-204.
- [8] Polverino P, Esposito A, Pianese C, Ludwig B, Iwanschitz B, Mai A. On-line experimental validation of a model-based diagnostic algorithm dedicated to a solid oxide fuel cell system. *J Power Sour* 2016;306: 646-657.
- [9] Ellamla HR, Staffel I, Bujlo P, Pollet BG, Pasupathi S. Current status of fuel cell based combined heat and power systems for residential sector. *J Power Sour* 2015;293:312–328.

- 1
2
3
4
5
6
7
8
9
10
11
12
13
14
15
16
17
18
19
20
21
22
23
24
25
26
27
28
29
30
31
32
33
34
35
36
37
38
39
40
41
42
43
44
45
46
47
48
49
50
51
52
53
54
55
56
57
58
59
60
61
62
63
64
65
- [10] Hagen A, Høgh JVT, Barfod R. Accelerated testing of solid oxide fuel cell stacks for micro combined heat and power application. *J Power Sour* 2015;300:223–228.
- [11] Napoli R, Gandiglio M, Lanzini A, Santarelli M. Techno-economic analysis of PEMFC and SOFC micro-CHP fuel cell systems for the residential sector. *Energy Build* 2015;103:131–146.
- [12] Pellegrino S, Lanzini A, Leone P. Techno-economic and policy requirements for the market-entry of the fuel cell micro-CHP system in the residential sector. *Appl Energy* 2015;143:370–382.
- [13] Facci AL, Cigolotti V, Jannelli E, Ubertini S. Technical and economic assessment of a SOFC-based energy system for combined cooling, heating and power. *Appl Energy* 2017;192:563–574.
- [14] Strezza C, Del Borghi A, Costamagna P, Traverso A, Santin M. Comparative LCA of methanol-fuelled SOFCs as auxiliary power systems on-board ships. *Appl Energy* 2010;87:1670–1678.
- [15] Diaz-de Baldasano MC, Mateos FJ, Nuñez-Rivas LR, Leo TJ. Conceptual design of offshore platform supply vessel based on hybrid diesel generator-fuel cell power plant. *Appl Energy* 2014;116:91–100.
- [16] Venkataraman V, Pacek AW, Steinberger-Wilckens R. Coupling of a Solid Oxide Fuel Cell Auxiliary Power Unit with a Vapour Absorption Refrigeration System for Refrigerated Truck Application. *Fuel Cells* 2016;16:273–293.
- [17] Kendall K, Newton J, Kendall M. Microtubular SOFC (mSOFC) System in Truck APU Application, *Electrochem Soc Trans* 2015;68:187–192.
- [18] Recheberg J, Kaupert A, Greisen C, Hagerskans J, Blum L. Fuel Cell Auxiliary Power Units for Heavy Duty Truck Anti-Idling. *SAE Int J Commer Veh* 2013;6:555–562.
- [19] He J, Xhou P, Clelland D. The development of control strategy for solid oxide fuel cell and micro gas turbine hybrid power system in ship application. *J Mar Sci Technol* 2014;19:462–469.
- [20] Larosa L, Ferrari ML, Magistri L, Massardo AF. SOFC/mGT Coupling: Different Options With Standard Boosters, *ASME Turbo Expo 2013: Turbine Technical Conference and Exposition*;2013 June 3–7; San Antonio, Texas, USA.
- [21] Santin M, Traverso A, Magistri L, Massardo A. Thermo-economic analysis of SOFC-GT hybrid systems fed by liquid fuels, *Energy* 2010;25:1077–1083.
- [22] Obara S. Dynamic-characteristics analysis of an independent microgrid consisting of a SOFC triple combined cycle power generation system and large-scale photovoltaics. *Appl Energy* 2015;141:19–31.

- 1
2
3
4
5
6
7
8
9
10
11
12
13
14
15
16
17
18
19
20
21
22
23
24
25
26
27
28
29
30
31
32
33
34
35
36
37
38
39
40
41
42
43
44
45
46
47
48
49
50
51
52
53
54
55
56
57
58
59
60
61
62
63
64
65
- [23] Zaccaria V, Tucker D, Traverso A. Transfer function development for SOFC/GT hybrid systems control using cold air bypass. *Appl Energy* 2016;165:695–706.
- [24] Sharifzadeh M, Meghdari M, Rashtchian D. Multi-objective design and operation of Solid Oxide Fuel Cell (SOFC) Triple Combined-cycle Power Generation systems: Integrating energy efficiency and operational safety. *Appl Energy* 2017;185:345–361.
- [25] Cinti G, Baldinelli A, Di Michele A, Desideri U. Integration of Solid Oxide Electrolyzer and Fischer-Tropsch: A sustainable pathway for synthetic fuel. *Appl Energy* 2016;162:308–320.
- [26] Bi L, Boulfard S, Traversa E. Reversible solid oxide fuel cells (R-SOFCs) with chemically stable proton-conducting oxides. *Sol State Ion* 2015;275:101–105.
- [27] Jung GB, Chang CT, Yeh CC, Nguyen XV, Chang SH, Lin CY, et al. Study of reversible solid oxide fuel cell with different oxygen electrode materials. *Int J Hydrogen Energy* 2016;41:21802–21811.
- [28] Terayama T, Momma A, Tanaka Y, Kato T. Improvement of Single Solid Oxide Fuel Cell Performance by Using Anode Off-Gas Recycling. *J Electrochem Soc* 2016;163:F1380-F1388.
- [29] Peters R, Deja R, Engelbracht M, Frank M, Nguyen VN, Blum L, et al. Efficiency analysis of a hydrogen-fueled solid oxide fuel cell system with off-gas recirculation. *J Power Sour* 216;328:105–113.
- [30] Henke M, Hillius S, Riedel M, Kallo J, Friendrich KA. Gas Recirculation at the Hydrogen Electrode of Solid Oxide Fuel Cell and Solid Oxide Electrolysis Cell Systems. *Fuel Cells* 2016;16:584–590.
- [31] Tallgren J, Thomann O, Halinen M, Himanen O, Kiviaho J. Development of a fuel feeder for a solid oxide fuel cell test station. *Int J Energy Res* 2015;39:2031–2041.
- [32] Curletti F, Gandiglio M, Lanzarini A, Santarelli M, Maréchal F. Large size biogas-fed Solid Oxide Fuel Cell power plants with carbon dioxide management: Technical and economic optimization. *J Power Sour* 2015;294:669–690.
- [33] Khani L, Mher AS, Yari M, Mahmoudi SMS. Multi-objective optimization of an indirectly integrated solid oxide fuel cell-gas turbine cogeneration system. *Int J Hydrogen Energy* 2016;41:21470–21488.
- [34] Sorce A, Greco A, Magistri L, Costamagna P. FDI oriented modeling of an experimental SOFC system, model validation and simulation of faulty states. *Appl Energy* 2014;136:894–908.

- 1
2
3
4
5
6
7
8
9
10
11
12
13
14
15
16
17
18
19
20
21
22
23
24
25
26
27
28
29
30
31
32
33
34
35
36
37
38
39
40
41
42
43
44
45
46
47
48
49
50
51
52
53
54
55
56
57
58
59
60
61
62
63
64
65
- [35] Greco A, Sorce A, Littwin R, Costamagna P, Magistri L. Reformer faults in SOFC systems: Experimental and modeling analysis, and simulated fault maps. *Int J Hydrogen Energy* 2014;39:21700–21713.
- [36] Costamagna P, De Giorgi A, Gotelli A, Magistri L, Moser G, Sciaccaluga E, et al. Fault Diagnosis Strategies for SOFC-Based Power Generation Plants. *Sensors* 2016;16:1336-1/17.
- [37] Pahon E, Yousfi-Steiner N, Jemei S, Hissel D, Péra MC, Wang K, et al. Solid oxide fuel cell fault diagnosis and ageing estimation based on wavelet transform approach. *Int J Hydrogen Energy* 2016;41:13687–13687.
- [38] Sorrentino M, Marra D, Pianese C, Guida M, Postiglione F, Wang K, Pohjoranta A. On the Use of Neural Network and Statistical Tools for Nonlinear Modeling and On-Field Diagnosis of Solid Oxide Fuel Cell Stacks. *Energy Procedia* 2014;45:298–307.
- [39] Pohjoranta A, Sorrentino M, Pianese C, Amatruda F, Hottinen T. Validation of neural network-based fault diagnosis for multi-stack fuel cell system: stack voltage deviation detection. *Energy Procedia* 2015;81:173–181.
- [40] Wu XJ, Liu H. Fault diagnosis of solid oxide fuel cell based on a supervised self-organization map model. *J Fuel Cell Sci and Technol* 2015;12:031001-1/8.
- [41] Marra D, Sorrentino M, Pohjoranta A, Pianese C, Kiviahio J. A lumped dynamic modelling approach for model-based control and diagnosis of Solid Oxide Fuel Cell system with anode off-gas recycling. *ECS Trans* 2015;68:3095–3106.
- [42] Halinen M, Pennanen J. Analysis of Leakages in a Solid Oxide Fuel Cell Stack in a System Environment. *Fuel Cells* 2014;15:434–444.
- [43] Marra D, Pianese C, Polverino P, Sorrentino M. Models for Solid Oxide Fuel Cell Systems – Exploitation of Models Hierarchy for Industrial Design of Control and Diagnosis Strategies. Springer;2016.
- [44] Simani S, Fantuzzi C, Patton RJ. Model-based Fault Diagnosis in Dynamic Systems Using Identification Techniques. Springer-Verlag; 2003.
- [45] Isermann R. Fault-diagnosis Systems an Introduction from Fault Detection to Fault Tolerance. Springer; 2006.

- 1
2 [46] Gao Z, Cecati C, Ding SX. A Survey of Fault Diagnosis and Fault-Tolerant Techniques-Part I: Fault
3 Diagnosis With Model-Based and Signal-Based Approaches. IEEE Trans Ind Electron 2015;62:3575–
4 3767.
5
6 [47] Veseley WE, Goldberg FF, Roberts NH, Haasl DF. Fault Tree Handbook. Washington, D.C, USA: U.S.
7 Nuclear Regulatory Commission;1981.
8
9 [48] Di Filippi A. Development and experimental validation of CPOx reforming dynamic model for fault
10 detection and isolation in SOFC systems. University of Salerno: Ph.D. Thesis; 2015.
11
12 [49] Larminie J, Dicks A. Fuel Cell Systems Explained. West Sussex, UK: John Wiley & Sons Ltd; 2003.
13
14 [50]
15
16
17
18
19
20
21
22
23
24
25
26
27
28
29
30
31
32
33
34
35
36
37
38
39
40
41
42
43
44
45
46
47
48
49
50
51
52
53
54
55
56
57
58
59
60
61
62
63
64
65